Optical fiber links for transmission of nanojoule femtosecond laser pulses

Olsson, Rasmus Kjelsmark

Publication date:
2010

Document Version
Publisher's PDF, also known as Version of record

Optical fiber links for transmission of nanojoule femtosecond laser pulses

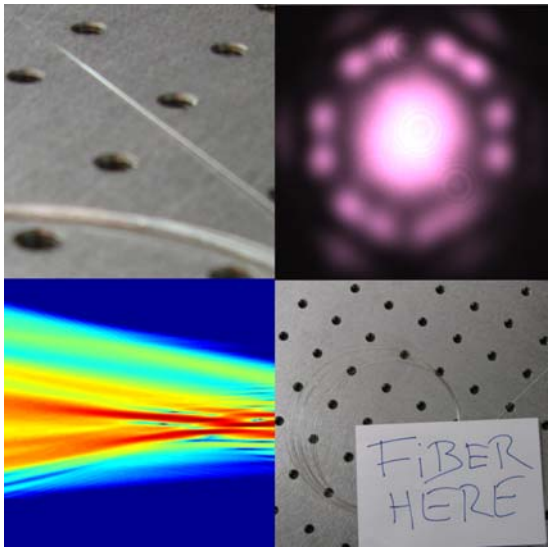

Ph.D. Thesis
Rasmus Kjelsmark Olsson
April 2010

DTU Fotonik
Department of Photonics Engineering

Optical fiber links for transmission of nanojoule femtosecond laser pulses

Ph.D. Thesis
Rasmus Kjelsmark Olsson
April 2010

Technical University of Denmark
DTU Fotonik - Department of Photonics Engineering
Lyngby, Denmark

Preface

In this thesis I present numerical and experimental results for optical fiber links that have been developed for transmission and compression of femtosecond laser pulses from fiber laser based systems. Numerical simulations of the pulse propagation in the fiber links are presented as well as experimental work done on the characterization of pulse propagation in optical fiber links using frequency-resolved optical gating (FROG). Fiber links for two specific applications are demonstrated. The first application is the transmission of nJ femtosecond laser pulses from a commercial 1550 nm fiber laser to a terahertz imaging setup for terahertz generation using photoconductive switches. This fiber link consists of standard single-mode fiber and dispersion-compensating fiber. The second fiber link was designed for compression of 1028 nm femtosecond pulses in hollow-core photonic bandgap fibers for subsequent supercontinuum generation in nonlinear photonic crystal fibers using femtosecond pulses. This has potential applications in all-fiber supercontinuum fiber laser systems. The use of hollow-core fiber allows compression with higher pulse peak power compared to standard single-mode fibers which have a silica glass core. For the experiments a single-polarization SESAM modelocked femtosecond fiber laser with a 1028 nm center wavelength was constructed with free-space pulse picking and amplification in ytterbium (Yb) fiber amplifiers. In addition to this, a setup for FROG measurements was built with the purpose of having a better pulse characterization tool available in the lab and a significant part of the Ph.D. work has been to explore how the FROG method can be used in the development of fiber based systems. In both fiber link applications the efficiency of the radiation generation, either terahertz radiation or supercontinuum radiation at optical frequencies, is much dependent on the input pulse duration and pulse shape and therefore a careful characterization of the optical pulses is necessary.

The work that I present in this thesis was done at NKT Photonics A/S, Birkerød, Denmark and at DTU Fotonik - Department of Photonics Engineering, Technical University of Denmark in the period from February 2007 to

April 2010. The project was part of a collaboration between the Terahertz Technologies and Biophotonics group at DTU Fotonik and NKT Photonics A/S, formerly Koheras A/S. The project was supervised by:

- Peter Uhd Jepsen, Ph.D. Habil., Professor, group leader, DTU Fotonik, Technical University of Denmark, Lyngby, Denmark
- Thomas V. Andersen, Ph.D., NKT Photonics A/S, Birkerød, Denmark

The work presented here would not have been possible without the help and support from many people. Most of the work was done by me but many people have helped me along the way and I would like to thank them all. First of all I would like to thank the technical and administrative staff at DTU Fotonik. It has been a pleasure working together with people from the institute. I would like to thank my colleagues from the research group, Kristian Nielsen, Jonas C. D. Buron, Finn Eichhorn and Uffe Møller for their help and for their company for the last three years. Finn Eichhorn and I worked together on the 1550 nm fiber link and Finn did quite a few of the fiber cutback measurements. Jonas Buron measured terahertz pulses with the fiber link. I would also like to thank professor Peter Uhd Jepsen for giving me the opportunity to learn about terahertz spectroscopy and imaging. For some time it appeared that whenever we tried something new in the labs at DTU Fotonik then the work had already been done by our colleagues at NKT Photonics A/S. Here I would like to thank Thomas V. Andersen from NKT Photonics A/S for being to the point and giving me a head start. I would like to thank both Thomas as well as Jens Kristian Lyngsøe, also from NKT Photonics A/S, for their great help and their many insightful comments. Finally, I would like to thank my family, Leonard, Vilbert and Dorte. I acknowledge Photonics Academy Denmark and NKT Photonics A/S for partial financial support.

Copenhagen, 25th of April 2010
Rasmus Kjelsmark Olsson

Resumé

Danish abstract

I denne afhandling præsenteres numeriske og eksperimentelle resultater for en række optiske fiberlinks, der er blevet udviklet med henblik på transmission og komprimering af femtosekund pulser fra fiberbaserede lasersystemer. Der præsenteres numeriske simuleringer af pulsudbredelse i optiske fibere samt eksperimentelle resultater, der viser hvorledes pulsudbredelsen i optiske fiberlinks kan karakteriseres ved hjælp af en metode kaldet frequency-resolved optical gating (FROG). Der præsenteres fiberlinks til to forskellige anvendelsesområder. Det ene anvendelse er transmission af nanojoule femtosekund laserpulser fra en kommerciel 1550 nm fiberlaser til et terahertz imaging setup (til at tage billeder med lys med frekvenser i terahertz-området) med henblik på at generere terahertz stråling ved hjælp af photoledende kredsløb. Dette fiberlink består af standard single-mode fiber og dispersionskompenserende fiber. Det andet fiberlink blev designet til kompression af femtosekund pulser ved 1028 nm i hulkerne fotoniske båndgabsfibere med efterfølgende generering af hvidt lys, et såkaldt supercontinuum, i en ikke-lineær fotonisk krystalfiber. Dette har potentiel anvendelse i et fiberlaser-system til hvidlys-generering bestående udelukkende af optiske fibere. Brugen af hulkerne-fiber gør det muligt at komprimere optiske pulser med højere pulsamplituder i forhold til komprimering i standardfiber med glaskerne. Til eksperimenterne blev der udviklet en modelocked femtosekund fiberlaser med en centerbølgelængde på 1028 nm med udstyr til udtagning af enkelte pulser samt yderligere forstærkning i ytterbium (yb) fiberforstærkere. Derudover blev der konstrueret et FROG-setup for at have et bedre apparat til pulskarakterisering i laboratoriet. I begge anvendelser af de to fiberlinks er effektiviteten af genereringen af stråling, både terahertzstråling og supercontinuum ved optiske frekvenser, meget afhængig af inputpulses varighed og pulsformen og derfor er en grundig beskrivelse af pulserne nødvendig.

Contents

CHAPTER 1

Introduction

The topic of this thesis is the transmission of very short, picosecond and femtosecond laser pulses with nanojoule pulse energies in optical fiber links. The fiber links are designed to deliver, and compress, laser pulses from fiber lasers in a few meters of optical fibers. This makes it possible to distribute pulses with nanojoule pulse energies to a receiver point in a convenient way. In this thesis we consider two specific applications. The first application is terahertz generation with 100 fs pulses from a 1550 nm fiber link. The second application is compression of 1028 nm pulses from a ytterbium fiber laser in hollow-core photonic bandgap fiber for supercontinuum generation in a nonlinear photonic crystal fiber. In both fiber link applications the efficiency with which new frequencies are generated depends on the input pulse duration and pulse shape and therefore a careful characterization of the optical pulses and the pulse propagation through the fiber link is necessary. Both dispersive effects, i.e. that different frequency components in the pulse travels at different velocities through the fiber, and nonlinear effects, i.e. the generation of new colors, or wavelengths, have to be considered. Since the pulse energy in a femtosecond pulse is distributed over a very short time span the peak power of the optical pulse can be very high. A low-power fiberlaser can easily generate pulses with several horsepowers of peak power.[1] The high optical peak powers promote nonlinear effects in the optical fibers and although the nonlinearity of silica is

[1] There are several definitions of a horsepower and it is typically defined to be between 735.5 to 750 watts. The horsepower is not recognized in the International System of Units (SI) [1].

not particularly high when compared to other materials it comes into play at these pulse energies. The nonlinear effects are also enhanced in optical fibers because the light propagates over longer distances.

In this chapter we give an introduction to the topic of the thesis and we comment on research results that are relevant for pulse compression and pulse transmission applications. In chapter 2 we describe pulse propagation in optical fibers in more detail and in chapter 3 we describe the experimental setup, a frequency-resolved optical gating (FROG) setup, used for pulse characterization. The main results of this thesis can be found in chapters 4-6. In chapter 4 we describe a modelocked 1028 nm fiber laser that was constructed for the experiments, and results on spectral broadening in standard single-mode fiber and pulse compression in a free-space grating compressor are presented. The 1028 nm fiber laser was used for the experiments presented in chapter 6 on compression of laser pulses in hollow-core photonic bandgap fibers. Results on supercontinuum generation with the pulses compressed in hollow-core fiber are presented as well. Single-channel and multi-channel fiber links for distribution of 1550 nm pulses from a commercial fiber laser are presented in chapter 5. Chapter 7 summarizes the main points of the thesis and is accompanied by an outlook. Further details on the pulse picking electronics used in the fiber laser setup can be found in appendix A, while appendix B contain notes on normalization of the pulse amplitude and the energy density spectrum. Appendix C contain a list of publications.

Introduction to the topic

By now, optical fibers have been used for many years for data transmission in telecom applications. Data is encoded in optical pulses that propagate in the optical fibers with very low losses. Here we consider pulses with higher pulse energies in the nanojoule range. Optical fibers are interesting to work with in the context of short pulses and they are fascinating to work with in the laboratory for a number of reasons. What one quickly discovers when working with short pulses and optical fibers is how easy it is to promote different nonlinear optical effects in optical fibers because of the high optical peak powers of the pulsed light. The author of this thesis once had the pleasure to attend a lecture by Robert Stolen where he describe how he and co-workers demonstrated many of these nonlinear effects in optical fibers in the 1970s. Compared to a free space setup there is less freedom in a fiber configuration for adjusting e.g. the intensity of the light at a specific point in the system or the polarization of the light, but once the fiber laser system is working it is much more compact and stable than its free-space counterpart. This is convenient and in daily use no maintaince is needed which is also important for industrial applications. Occasionally, fiber laser components can get damaged by the high light intensities and this is one of the weak points in fiber based systems.

There are of course also some challenges when working with such short pulses. First of all, how are the optical pulses measured? The pulses are so short that no electronics is fast enough for the purpose. The most common ways to experimentally characterize optical pulse in the laboratory is to measure the spectrum of the optical pulses and to measure the intensity autocorrelation. In this thesis we describe how more information about the pulse can be obtained in a spectrally resolved autocorrelation type measurement known as *frequency-resolved optical gating* (FROG). Measuring short pulses is somewhat of a detectives job and the best results are often obtained by measuring not only a single pulse but many related pulses with different powers or with different frequency chirp and comparing the measurements to get a consistent picture of what is going on.

Comparison of different types of optical fibers

We are now going to present one of our workhorses, the optical fiber, and we consider three very different types of optical fibers. The fiber parameters are shown in table 1.1 below. The fiber *SMF-28* (Corning, SMF-28e) is a standard single-mode fiber used for telecommunication. The fiber complies with a specific set of requirements for telecommunication fibers (ITU-T G.652). The fiber *NL-1065* (NKT Photonics A/S, NL-5.0-1065) is a nonlinear photonic crystal fiber with a 5.0 μm core diameter [2]. Nonlinear fibers typically have a very small core diameter, down to 1 μm, which results in a very small effective area A_{eff} and therefore a high nonlinear parameter γ. For this fiber the nonlinear parameter γ is 11 W^{-1}/km and many nonlinear fibers have values above 100 W^{-1}/km but also much higher losses. Nonlinear fibers are used for supercontinuum generation, Raman amplification and four-wave mixing using e.g. Nd:YAG pump lasers at around 1060 nm [3]. Most of these nonlinear processes, e.g. four-wave mixing, are only efficient if specific phase-matching conditions are satisfied. There are different techniques for phase-matching the light at the pump wavelength with the light at some desired wavelength, e.g. using different modes in multimode fibers or phase-matching light with different polarizations in birefringent fibers [4]. Other nonlinear fibers have been designed with a zero dispersion around 800 nm suitable for pumping using Ti:Sapphire lasers. The fiber *HC-1060-02* (NKT Photonics A/S, HC-1060-02) is a hollow-core photonic bandgap fiber [5]. More than 95% of the optical power is located in the air-regions of the hollow-core fiber and the nonlinear coefficient is therefore very small because of the very low nonlinear refractive index of air. The fiber is used for pulse compression around 1060 nm where the slope of the dispersion curve is low and it can be used with high optical powers since most of the light travels in air. The fiber can also be used for sensing applications if the core of the fiber is filled with a gas [6, 7]. For all fibers the dispersion and the loss changes with the wavelength because of material dispersion and waveguide dispersion,

i.e. dispersion determined by the specific geometry of the waveguide. This is especially true for the hollow-core fiber which is a photonic band gap fiber with a transmission gap of around 100 nm.

	SMF-28	NL-1065	HC-1060-02
Loss, α	0.2 dB/km at 1550 nm 0.34 dB/km at 1310 nm	16 dB/km at 1064 nm	85 dB/km at 1060 nm
Group velocity dispersion, β_2	-20 ps^2/km at 1550 nm	7 ps^2/km at 1000 nm -7 ps^2/km at 1100 nm	15 ps^2/km at 1000 nm -110 ps^2/km at 1100 nm
Zero dispersion wavelength, λ_{ZD}	1312 nm $\pm$ 10 nm	1060 nm $\pm$ 10 nm	1010 nm $\pm$ 10 nm
Nonlinearity, γ	1 W^{-1}/km	11 W^{-1}/km	< 0.01 W^{-1}/km
		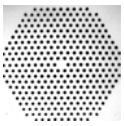	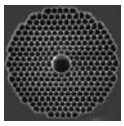

Table 1.1: Parameters for selected fibers.

The move from low power transmission in standard silica fibers to delivery of high optical powers in hollow-core fibers

Delivery of nanojoule femtosecond laser pulses via fiber has many applications in multi-photon microscopy [8], terahertz spectroscopy [9], terahertz imaging [10] and femtosecond laser systems. All-fiber pulse compression schemes are of interest for fiber amplifier systems where they can replace bulk optics prism or grating compressors.

Dispersion management has been investigated extensively for telecommunication applications as described in a review on dispersive compensating fibers (DCF) by **Grüner-Nielsen *et al.*** [11]. Dispersion management of femtosecond pulses in the linear regime using dispersion-compensating fiber (DCF) at 1300 nm to 1700 nm wavelength has originally been proposed by **Lin *et al.*** [12]. **Chang *et al.*** [13] demonstrated nearly dispersion-free transmission of sub-100-fs pulses in the low picojoule energy range over a 42 m concatenated

single-mode fiber (SMF) - DCF fiber link. In this and similar dispersion compensation experiments the idea is to match the dispersion of the SMF with the dispersion of a piece of DCF that has the same magnitude but is opposite in sign. For very short pulses or long fiber lengths the third-order dispersion (TOD) has to be efficiently compensated as well. Since the pulse peak power in these experiments was low, nonlinear effects were negligible.

Pulse delivery of nanojoule femtosecond pulses through large-mode-area (LMA) fibers has been demonstrated by **Ouzounov *et al.*** [14]. Here 3 nJ prechirped input pulses were compressed to 140 fs, and it was demonstrated that LMA fiber under the same conditions delivered 10 times shorter pulses than standard SMF due to reduced self-phase modulation (SPM). Recent work on pulse delivery of sub-100-fs, $<$ 800 nm pulses with microjoule pulse energies in specialty hollow core photonic crystal fiber has been demonstrated by **Skibina *et al.*** [15].

Hollow-core fibers are well suited for transmission of high energi pulses because of the low nonlinearity of the fibers [16]. The dispersion of hollow-core fibers is predominantly determined by the waveguide geometry and the dispersion can therefore be tailored to some extent. The dispersion can be anomalous below 1300 nm where silica fibers have normal dispersion and hollow-core fibers are produced with anomalous dispersion both at 800 nm, suitable for use with solid-state Ti:sapphire lasers, and at 1030-1060 nm for use with ytterbium fiber lasers. As mentioned above, the dispersion can be very high compared to the dispersion of standard fibers. Accurate measurements of the dispersion of hollow-core fibers are still being pursued and **M. G. Welch *et al.*** recently reported on precise measurements of the dispersion and the dispersion slope at both 800 nm and 1064 nm [17].

M. G. Welch *et al.* investigated soliton compression in tapered hollow-core fiber and were able to compress a picosecond input pulse by over an order of magnitude [18]. In the experiment they tried to increase the nonlinearity by changing the geometry of the hollow-core fiber to fill the gap, of several orders of magnitude, in nonlinearity between silica fibers and hollow-core fibers. This would allow the transmission of solitons with intermediate pulse energies in the nanojoule range. However, they found that an increase in nonlinearity also increased the dispersion such that the reduction in soliton energy was only a factor of approximately 2. In the following we describe hollow-core fibers and pulse compression in more detail.

Hollow-core fibers

Hollow-core fibers potentially have lower fiber transmission losses than silica fibers because most of the light in a hollow-core fiber, typically more than 95%, propagates in air. In standard fiber the most important reasons for transmission losses are material absorption and Rayleigh scattering. Standard silica fibers

have a mimimum loss of about 0.2dB/km at 1.55 μm and such low losses are difficult to reach with hollow-core fibers. Recently **J. K. Lyngsøe *et al.*** reported on the fabrication of several 7-cell core hollow-core photonic crystal fibers with low losses in the spectral range from 1.4 μm to 2.3 μm [19]. One of the fibers that was reported on had a transmission loss of 26 dB/km at 2.3 μm which is very low compared to the fiber loss of standard silica fibers at this wavelength. One of the reasons why it is difficult to reach low losses in hollow-core fibers is that light can be scattering by the silica walls in the cladding. Another reason is that it is difficult to manufacture a photonic bandgap of sufficient quality to keep the light in the air core. In comparison, light is very strongly confined by total internal reflection in silica with an air-cladding because of the large contrast in refractive indices.

Light with different polarization states typically propagate at slightly different velocities in optical fibers because of birefringence. Some fibers have a rotational symmetry and are designed such that birefringence is minimized, there will, however, always be some random birefringence caused by imperfections in the fiber or bending of the fiber which can lead to *polarization mode dispersion*. Polarization mode dispersion can have a severe effect on the quality of data transmission in optical fiber links at high data rates and over long distances because light in different polarization modes are transmitted at different velocities. Other fibers are designed to have a high builtin birefringence and are *polarization maintaining (PM)*. In general, hollow-core fibers have a tendency to be birefringent because they are difficult to manufacture such that there is a rotational symmetry, the core can be slightly elliptical for example, and the birefringence of a hollow-core fiber, which was not intented to be birefringent in the first place, can be on the order of $\Delta n \sim 10^{-4}$ which is comparible to the birefingence of standard PM fiber, e.g. $\Delta n \sim 3 \cdot 10^{-4}$ for the Nufern PM Panda fiber PM980-HP. Structural imperfections and stress in the fiber lead to random birefringence and therefore to polarization mode dispersion. If linear polarized light is coupled into one of the polarization axes of a birefringent fiber then it will stay in this polarization mode to a certain degree. There will still be some coupling between the polarization modes because of fiber imperfections, stress in the fiber because of bending etcetera but this is suppresed to some extent. The *polarization extinction ratio* (PER) is a measure of the degree of linear polarized light and it is defined as the ratio of optical powers in the two polarization directions. One way to make a hollow-core fiber birefringent intentionally is to use an elliptical core. Another solution is to place either two or four localized, antiresonant features asymmetrically on the core wall to create an axis of birefringence in the fiber as demonstrated by **B. Mangan *et al.*** [20]. **J. K. Lyngsøe *et al.*** reported on a birefringent solid-core photonic crystal fiber that guided by a combination of bandgap mechanisms and total internal reflection [21].

Pulse compression and transmission in hollow-core photonic bandgap fibers

Transmission of megawatt peak power solitons in hollow-core fiber were reported by **Dimitre G. Ouzounov *et al.*** [22]. In this important experiment femtosecond solitons with 2 megawatt peak powers were delivered in an air-filled fiber and solitons with 5.5 megawatt peak power were delivered in a xenon-filled fiber. The fiber was filled with xenon such that the soliton would not shift to longer wavelengths because of Raman scattering. **F. Luan *et al.*** reported on similar results and in their experiment femtosecond solitons at 800 nm were delivered over 5 m hollow-core fiber [23]. The pulses in their experiment were compressed to less than 300 fs with a pulse energy of 65 nJ. The couling efficiency into the fiber was around 30% and they observed damage to the fiber end facets when the pulse energy was around 320 nJ. Soliton compression in a tapered hollow-core fiber was reported by **F. Gérôme *et al.*** [24]. In the *soliton compression* scheme a fundamental soliton propagates along a fiber with a continuous decreasing group-velocity dispersion. The nonlinearity of the fiber and the soliton energy remain almost constant and the decrease in dispersion causes the soliton to compress (cf. eq. 2.22) if the change in dispersion is small. In the experiment by F. Gérôme *et al.* an unchirped 195 fs input pulse at 800 nm was compressed to less than 100 fs after 8 m of fiber. In a later experiment F. Gérôme *et al.* demonstrated how the Raman self-frequency shift of solitons at 1064 nm in a hollow-core fiber could be used for a tunable femtosecond soliton source [25]. The solitons were redshifted depending on the input pulse energy.

Next, we consider the use of hollow-core fiber for dispersive compression in fiber lasers. One technical challenge is to fusion splice hollow-core fiber to the other types of optical fibers because the optical modes in the fibers differ and because the photonic crystal structure in the hollow-core fiber cladding is fragile and there is only very little glass in the cladding to splice to. Low-loss fusion splicing of polarization-maintaining single-mode fiber and hollow-core photonic crystal fibers was reported by **J. T. Kristensen *et al.*** [26]. The authors reported splicing losses of 0.62 dB from SM fiber to HC-PCF and 2.19 dB from HC-PCF to SM fiber. The discrepancy was explained by the mode evolution in the hollow-core fiber. The polarization extinction ratio was 19 dB. A high polarization extinction ratio for the spliced fibers make it possible to use hollow-core fiber in laser applications where polarization effects, e.g. cross-phase modulation, have to be minimized. Birefringent fibers can by used with linear polarized light for pulse compression of light in one polarization mode. **D. Turchinovich *et al.*** demonstrated dispersive compression of chirped femtosecond pulses from an all-polarization-maintaining (PM) Yb-fiber laser in a hollow-core photonic crystal fiber (HC-1060-02, NKT Photonics A/S) [27]. The system delivered 4 nJ, 370 fs pulses and was monolithic in the sense that it was

made from fiber and fiber components spliced together without any free-space components. The femtosecond fiber laser system used by D. Turchinovich and co-workers is similar to the Yb-fiber laser that is used for the pulse compression experiment described in chapter 6 of this thesis and it is the same hollow-core fiber, HC-1060-02, that is being used.

Compression of linearly chirped picosecond pulses in hollow-core photonic bandgap fibers have been investigated numerically by **J. Lægsgaard *et al.*** considering both parabolic pulses [28] and more realistic pulses from fiber-based master-oscillator power-amplifer (MOPA) systems with pulse energies from 0.1 μJ to 1.8 μJ [29]. The parabolic input pulses were found to be more superior for obtaining high-quality compressed pulses at moderate pulse energies while there was not a significant difference at high output peak powers in MW range. J. Lægsgaard *et al.* also investigated the influence on the air pressure in the hollow-core fiber and found that a reduction in the air pressure lead to an increase in the fraction of energy that went into the most redshifted soliton [30, 31].

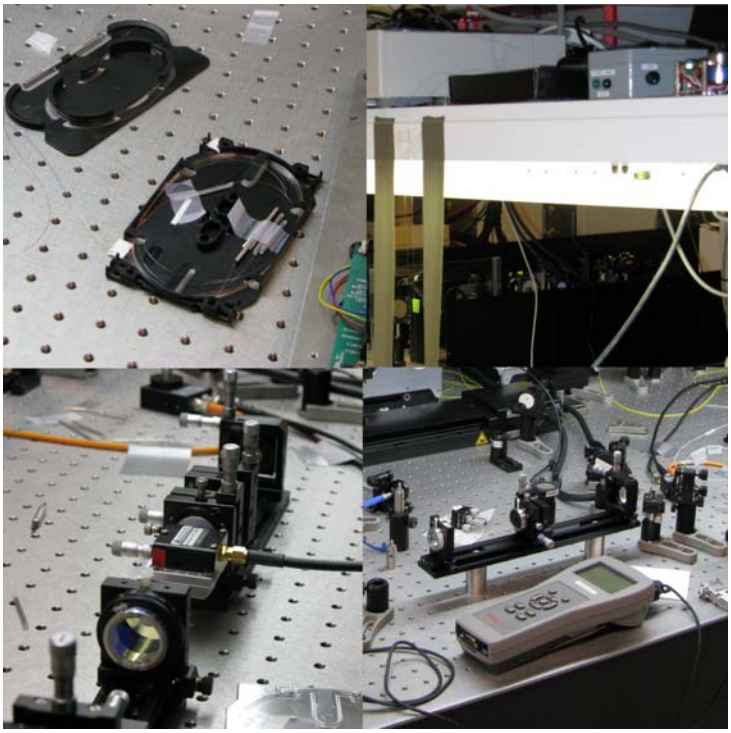

Figure 1.1: Photographs from the laboratory showing fiber amplifiers (top, left), fiber oscillator and pre-amplifier (top, right), free space setup for pulse picking (bottom, left) and the main part of the FROG pulse characterization setup (bottom, right). The fiber oscillator and a pre-amplifier are located on the shelf above the optical table and is connected to the rest of the laser system through optical fibers (the fibers go along the pieces of duct tape).

CHAPTER 2

Theory of pulse propagation in optical fibers

In this chapter we give an introduction to the theory on pulse propagation in optical fibers. We introduce the expressions needed for numerical simulations of femtosecond and picosecond laser pulse propagation with specific attention to the generalized nonlinear Schrödinger equation (GNLSE). The most important feature of an optical fiber is that it is a very long waveguide and that light can be guided over long distances with low losses. This also implies that the interaction length between light and fiber is very long. At the same time the dimensions of the fiber core is on the order of a few μm and this is where most of the intensity of the light is located and guided. The combination of a long interaction length and high intensities promote nonlinear effects. Nonlinear effects are minimized in hollow-core fibers because the light propagates in the air core of the fiber. In this chapter we only consider the nonlinear response of a standard silica fiber. For hollow-core fibers there are models that take the relative distribution of light in glass and air into account and include the Raman response of air [32]. The different effects and how they work together has been well described in a textbook by G. Agrawal [4]. At the end of the chapter we give an example of numerical simulations when we look at pulse compression and pulse breakup in standard single-mode fiber.

2.1 Description of ultrashort light pulses

The electric field of a light pulse can be written in time domain as

$$E(t) = \mathrm{Re}\left(\sqrt{I\,(t)}e^{i(\omega_0 t - \phi(t))}\right), \tag{2.1}$$

where $I(t)$ is the intensity, or envelope, of the pulse and $\phi(t)$ is the time-varying phase of the pulse. The carrier frequency of the pulse is ω_0. The instantaneous frequency of the pulse is given by

$$\omega_{\mathrm{inst}}(t) = \omega_0 - \frac{d\phi(t)}{dt} \tag{2.2}$$

If the instantaneous frequency changes across the pulse then we say that the pulse is *chirped*. If the phase $\phi(t)$ simply changes linearly across the pulse then it corresponds to a constant shift in frequency and the pulse is not chirped. A quadratic phase in time amounts to a linear change in frequency across the pulse and the pulse is linearly chirped. In the frequency domain the pulse follows from the Fourier transform and is given by

$$E_f(\omega) = \mathrm{Re}\left(\sqrt{I_f\,(\omega-\omega_0)}e^{i\phi_f(\omega-\omega_0)}\right), \tag{2.3}$$

where $I_f(\omega-\omega_0)$ is the optical power spectrum of the pulse and $\phi_f(\omega-\omega_0)$ is the spectral phase.

2.2 Propagation equation

The propagation of an optical pulse in a single-mode fiber is described by the generalized nonlinear Schrödinger equation [4]

$$\begin{aligned}\frac{\partial A}{\partial z} = &-\frac{1}{2}\left(\alpha(\omega_0) + i\alpha_1\frac{\partial}{\partial t}\right)A - \beta_1\frac{\partial A}{\partial t} - \frac{i\beta_2}{2}\frac{\partial^2 A}{\partial t^2} + \frac{\beta_3}{6}\frac{\partial^3 A}{\partial t^3}\\ &+ i\left(\gamma(\omega_0) + i\gamma_1\frac{\partial}{\partial t}\right)\left(A(z,t)\int_0^\infty R(t')|A(z,t-t')|^2 dt'\right)\end{aligned} \tag{2.4}$$

where $A(z,t)$ is the slowly varying pulse envelope. The amplitude is normalized such that $|A(z,t)|^2$ is the optical power $P(z,t)$. We describe the different terms in the paragraphs that follow. An approximation to the nonlinear Schrödinger equation is given by

$$\begin{aligned}&\frac{\partial A}{\partial z} + \frac{\alpha}{2}A + \frac{i\beta_2}{2}\frac{\partial^2 A}{\partial T^2} - \frac{\beta_3}{6}\frac{\partial^3 A}{\partial T^3}\\ &= i\gamma\left(|A|^2 A + \frac{i}{\omega_0}\frac{\partial}{\partial T}(|A|^2 A) - T_R A\frac{\partial |A|^2}{\partial T}\right)\end{aligned} \tag{2.5}$$

where T is the time relative to a frame moving with the pulse at the group velocity v_g

$$T = t - z/v_g \equiv t - \beta_1 z \tag{2.6}$$

We will be using both expressions in the following. The approximation is valid for pulses that are a few hundred femtoseconds or longer depending on the pulse bandwidth.

Fiber loss

The loss rate α is defined such that the change in the amplitude caused by losses is given by

$$\frac{dA}{dz} = -\frac{1}{2}\alpha A \tag{2.7}$$

or

$$A(z,t) = A(0,t)e^{-\frac{1}{2}\alpha z}$$

The loss is dependent on the frequency ω and a Taylor expansion of α around a center frequency ω_0 gives

$$\alpha(\omega) = \alpha(\omega_0) + \alpha_1(\omega - \omega_0) + \frac{\alpha_2}{2}(\omega - \omega_0)^2 + \cdots \tag{2.8}$$

The first two terms $\alpha(\omega_0)$ and α_1 are included in the propagation equation and higher-order terms can be added when needed. The loss terms can be neglected when the loss is low compared to the length of the fiber. The loss is often specified as

$$\alpha_{\mathrm{dB}}^{\mathrm{km}} = 10 \cdot \log_{10}\left(\frac{\mathrm{P_{in}(1km)}}{\mathrm{P_{out}(1km)}}\right) \tag{2.9}$$

with the unit dB/km. We see that α is related to $\alpha_{\mathrm{dB}}^{\mathrm{km}}$ by

$$\alpha = \alpha_{\mathrm{dB}}^{\mathrm{km}} \ln(10) 10^{-4}, \tag{2.10}$$

with α in SI units.

Dispersion

The term containing β_1 describe the linear refraction and it disappears when the time is measured in a frame of reference moving with the group velocity v_g.

The terms containing β_2 and β_3 describe the dispersion, i.e. how the phase velocity varies with frequency. They come from a Taylor expansion of the propagation constant $\beta(\omega)$ around the carrier frequency ω_0

$$\beta(\omega) = \beta_0 + \beta_1(\omega - \omega_0) + \frac{\beta_2}{2}(\omega - \omega_0)^2 + \frac{\beta_3}{6}(\omega - \omega_0)^3 + \ldots \tag{2.11}$$

where

$$\beta_m = \left(\frac{d^m\beta}{d\omega^m}\right)_{\omega=\omega_0} \qquad m = 1, 2, \ldots \tag{2.12}$$

Here $\beta_1 = v_g^{-1}$ is the reciprocal group velocity and β_2 describes how β_1 changes with frequency and is therefore called the group velocity dispersion (GVD). The higher order dispersion is described by β_3 (the third order dispersion, TOD), β_4 etcetera.

The higher order terms can be neglected for long pulses. However, they have to be included when the pulse has a broad spectrum and we can see that the third order dispersion contributes as much as the group velocity dispersion to the propagation constant when

$$\frac{\beta_3}{3}(\omega - \omega_0) = \beta_2$$

Similar expressions can be found for the other higher order contributions. For some types of fiber like the photonic crystal fibers the higher order terms can be large compared to standard fibers.

The higher order terms also have to be included when the pulse spectrum includes the zero-dispersion wavelength of the fiber. At the zero-dispersion wavelength β_2 becomes zero and at least β_3 has to be included.

Often the dispersion parameter D is used instead of β_2. It is related to β_2 by

$$D \equiv \frac{d\beta_1}{d\lambda} = -\frac{2\pi c}{\lambda^2}\beta_2 \tag{2.13}$$

The dispersion parameter D has the unit ps/nm/km.

Nonlinear effects

The last term in the propagation equation (eq. 2.4) describe the intensity-dependent nonlinear effects. The nonlinear parameter γ is given by

$$\gamma(\omega) = \frac{n_2(\omega)\omega}{cA_{\text{eff}}} \tag{2.14}$$

where $n_2(\omega)$ is the nonlinear-index coefficient at frequency ω, c is the speed of light in vacuum and A_{eff} is the effective mode area which is defined by

$$A_{\text{eff}} = \frac{\left(\int\int_{-\infty}^{\infty} |F(x,y)|^2 dxdy\right)^2}{\int\int_{-\infty}^{\infty} |F(x,y)|^4 dxdy} \tag{2.15}$$

where $F(x, y)$ is the traverse modal distribution of the fiber mode. The parameters $\gamma(\omega_0)$ and γ_1 are the first two expansion coefficients in the expansion of

γ around the center wavelength ω_0

$$\gamma(\omega) = \gamma(\omega_0) + \gamma_1(\omega - \omega_0) + \frac{1}{2}\gamma_2(\omega - \omega_0)^2 + \cdots$$

The nonlinear refractive index of fused silica is around

$$n_2 = 2.4 \times 10^{-20}\mathrm{m}^2/\mathrm{W}$$

while for air

$$n_2^{\mathrm{air}} = 2.9 \times 10^{-23}\mathrm{m}^2/\mathrm{W}$$

These are approximate numbers and wavelength dependent. The nonlinear response function $R(t)$ is given by

$$R(t) = (1 - f_R)\delta(t - t_e) + f_R h_R(t), \tag{2.16}$$

where f_R is the fraction of the response which comes from the Raman response. The Raman response can be approximated by the equation

$$h_R(t) = \frac{\tau_1^2 + \tau_2^2}{\tau_1 \tau_2^2} \exp(\frac{-t}{\tau_2}) \sin(\frac{t}{\tau_1}). \tag{2.17}$$

The first part of the response is a fast response described by the delta function $\delta(t - t_e)$. The response $R(t)$ reduces to this delta function when there is no Raman scattering, $f_R = 0$. The values $\tau_1 = 12.2$ fs, $\tau_2 = 32$ fs and $f_R = 0.18$ have been found experimentally. If we insert the response function in the propagation equation then we can rewrite the nonlinear term as

$$\begin{aligned}
&i\left(\gamma(\omega_0) + i\gamma_1\frac{\partial}{\partial t}\right)\left(A(z,t)\int_0^\infty \left[(1-f_R)\delta(t'-t_e) + f_R h_R(t')\right]|A(z,t-t')|^2 dt'\right) \\
&= i\left(\gamma(\omega_0) + i\gamma_1\frac{\partial}{\partial t}\right)\left((1-f_R)A(z,t)|A(z,t-t_e)|^2\right. \\
&\quad \left. + f_R A(z,t)\int_0^\infty h_R(t')|A(z,t-t')|^2 dt'\right) \\
&\approx (1-f_R)\left(i\gamma(\omega_0)A(z,t)|A(z,t)|^2\right) - (1-f_R)\left(\gamma_1\frac{\partial}{\partial t}\left(A(z,t)|A(z,t)|^2\right)\right) \\
&\quad + if_R\left(\gamma(\omega_0) + i\gamma_1\frac{\partial}{\partial t}\right)\left(A(z,t)\int_0^\infty h_R(t')|A(z,t-t')|^2 dt'\right)
\end{aligned} \tag{2.18}$$

At a first glance it seems that the SPM is reduced by the factor $(1 - f_R)$ compared the the amount of SPM without Raman scattering where $f_R = 0$. However, if we make a Taylor expansion of the intensity (with t' as the expansion variable and expand around $t' = 0$)

$$|A(z,t-t')|^2 = |A(z,t)|^2 - t'\frac{\partial}{\partial t}|A(z,t)|^2 + \cdots$$

and insert the two first terms in eq. (2.18) we get

$$\begin{aligned} i\gamma(\omega_0)A(z,t)|A(z,t)|^2 - \gamma_1\frac{\partial}{\partial t}\left(A(z,t)|A(z,t)|^2\right) \\ -i\left(\gamma(\omega_0) + i\gamma_1\frac{\partial}{\partial t}\right)T_R A(z,t)\frac{\partial}{\partial t}|A(z,t)|^2 \end{aligned} \tag{2.19}$$

where it was used that

$$\int_0^\infty h_R(t)dt = 1,$$

and where T_R is defined by

$$T_R \equiv \int_0^\infty tR(t)dt \approx f_R \int_0^\infty t h_R(t)dt.$$

T_R is determined experimentally to be around 3 fs. The first term in eq. (2.19) describe self-phase modulation (SPM), the second self-steepening, and the third Raman scattering. Now we see that there was an instantaneous response contribution from $h_R(t)$ and that the SPM and self-steepening terms are independent of the amount of Raman scattering. This approximation is only valid when the pulse is long compared to the Raman response, cf. fig. 2.1. However, higher order terms can be included through the Taylor expansion when needed and the expansion will always contain the first order term $|A(z,t)|^2$ which amounts to an instantaneous response. For very long pulses the Raman response becomes negligible.

Different propagation regimes

Given a fiber with parameters α, β and γ the importance of dispersion and nonlinear effects is determined by the peak power of the propagating pulse P_0, the pulse width T_0, or the spectral width, and the length L of the fiber. The pulse width T_0 is defined such that $2T_0$ is the e^{-1} width of the pulse. This is related to the FWHM of the pulse by

$$T_{\text{FWHM}} = 2(\ln 2)^{1/2}T_0 \approx 1.665T_0$$

Dispersion starts to be important when the fiber length is comparable to the dispersion length

$$L_D = \frac{T_0^2}{|\beta_2|},$$

Third order dispersion has to be included when

$$\frac{\beta_3}{3}(\omega - \omega_0) = \beta_2$$

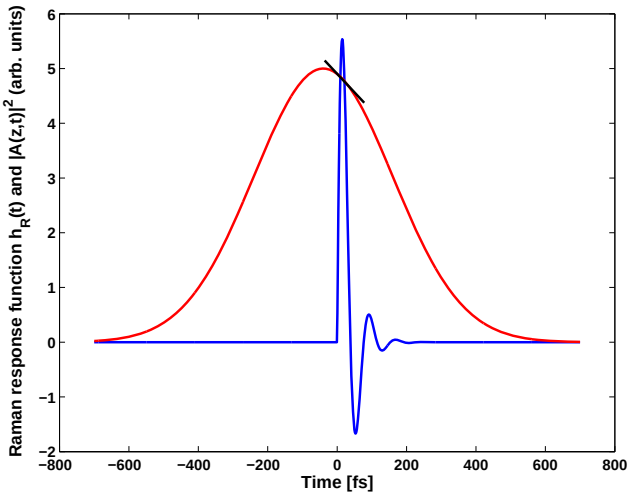

Figure 2.1: Illustration of the Raman response function $h_R(t)$ (blue line) and a pulse with pulse width $T_0 = 200$ fs (red line). The slope at $t' = 0$ i.e. $\frac{\partial}{\partial t}|A(z,t)|^2$ is also shown.

and similar for the higher order effects. The dispersion length in the absence of β_2 is given by:

$$L'_D = \frac{T_0^3}{|\beta_3|} \tag{2.20}$$

The nonlinear effects become important when the fiber length is comparable to

$$L_{\mathrm{NL}} = \frac{1}{\gamma P_0}$$

The nonlinear effects are dominant when

$$\frac{L_D}{L_{\mathrm{NL}}} \gg 1$$

For long pulses, typically longer than 1 ps, third order dispersion, self-steepening and Raman scattering are small effects that can be neglected. If dispersion is assumed to be negligible and only SPM is included then the solution to the propagation equation is

$$A(z,t) = A(z,0)\exp\left(i\gamma(\omega_0)|A(z,t)|^2 z\right) = A(z,0)\exp\left(i\phi_{\mathrm{NL}}(z,t)\right) \tag{2.21}$$

We see that the nonlinear phase change $\phi_{\mathrm{NL}}(z,t)$ depends on the intensity and it grows linearly with fiber length. For $L = L_{\mathrm{NL}}$ the phase will have changed

1 rad at the middle of the pulse where the intensity is highest. The change of the instantaneous frequency, i.e. the chirp added to the pulse, is given by

$$\delta\omega(t) = -\frac{\partial\phi_{\mathrm{NL}}}{\partial t} = -\gamma(\omega_0)z\frac{\partial}{\partial t}|A(z,t)|^2.$$

Solitons (bright solitons) require that the dispersion is anomalous, $\beta_2 < 0$. The peak power P_0 required to support the fundamental soliton is

$$P_0 = \frac{|\beta_2|}{\gamma T_0^2}$$

The soliton order N is given by:

$$N^2 = \frac{L_D}{L_{NL}} = \frac{T_0^2\gamma P_0}{|\beta_2|}. \tag{2.22}$$

We do not see solitons in the measurements that are presented in this thesis. The pulse energies are often high enough for creating a soliton but the pulses we encounter are chirped initially and they break up into several pulses before they can form a soliton. We will describe this process further below.

2.3 Numerical simulations of pulse propagation

The generalized nonlinear Schrödinger equation (eq. 2.4) can be solved numerically using the *split-step Fourier method* [4]. The equation is solved by propagating the pulse in small steps and for each step calculating the effects of dispersion and nonlinearity. For a small step size dispersion amounts to a simple multiplication in Fourier space of the pulse and a factor containing the dispersion. The nonlinear contribution is integrated in time domain. This method is typically much faster than solving the equation with finite-difference techniques. We use a freeware software package, SSPROP [33] that solves the GNLSE using the split-step method. The SSPROP functions are available in both a scalar and a vector version and we use the scalar version here because the nonlinear Schrödinger equation considered here only accounts for one polarization direction. SSPROP uses the simple approximation for the Raman response and the optical self-steepening. The calling syntax is

```
u1 = sspropc(u0,dt,dz,nz,alpha,betap,gamma,tr,to)
```

where `u0` and `u1` are number arrays containing the input and output pulses respectively, dt is the time between two points in the pulse arrays (such that the time window is given by `dt` times the number of points in the pulse arrays), `dz` is the integration step size and `nz` is number of integration steps. The other parameters `alpha, betap, gamma, tr` and `to` are the fiber parameters mentioned above.

2.4 Example: Propagation in anomalous dispersive fiber

As an example of how we use the numerical tools to simulate pulse propagation we consider the compression of a chirped nJ femtosecond pulse in anomalous dispersive fiber. The example will also illustrate a specific kind of pulse breakup which is relevant for the pulse transmission and pulse compression experiments presented in chapter 5.

We assume that the input pulse is a linearly chirped Gaussian pulse at 1550 nm with pulse width $\mathrm{T_{FWHM}} = 1$ ps, chirp parameter $C = -10$ and pulse energy $\mathrm{E_{pulse}} = 3.0$ nJ. The pulse can be expressed as [4]

$$U(T) = \exp\left(-\frac{(1+iC)}{2}\frac{T^2}{T_0^2}\right), \tag{2.23}$$

where $U(T)$ is the amplitude at time T. The fiber that is used in this example resembles a standard single-mode fiber (SMF) with anomalous dispersion at 1550 nm. Figures 2.2a-d show numerical simulations of the pulse propagating through the fiber when β_3 and γ in turn are set to zero. The pulse is chirped at the input such that red frequency components can be found in the leading part of the pulse, i.e. for negative times, and blue frequency components can be found in the trailing part of the pulse. If the chirp was opposite then the pulse would not be compressed in the fiber but instead become broader. Figure 2.2a shows how the pulse is compressed due to dispersion alone. In figure 2.2b third-order dispersion is included as well. A positive β_3 causes oscillations at the trailing end of the pulse no matter what the sign of β_2 is [4]. The oscillations disappear when the effect of β_3 gets small compared to the effect of β_2, i.e. this depends on the pulse bandwidth. Figure 2.2c shows the combined effect of dispersion and SPM. The dispersive compression takes place faster at the center of the pulse because of the intensity dependent SPM induced chirp and the pulse breaks up into several pulses. This occurs at a much earlier position in the fiber compared to the case where the pulsed is compressed by dispersion alone. The low-power tails of the pulse are compressed at a slower rate. In figure 2.2d third-order dispersion is included again. The compression is now asymmetric over the pulse because of third-order dispersion. Figures 2.3a-e show the pulse intensity and phase for different fiber lengths in the case where both third-order dispersion and SPM are included.

The most important mechanism in this example is the interplay between group velocity dispersion and SPM. In the example the nonlinear length was comparable to the dispersive length ($L_\mathrm{D} = 0.16$ m using the pulse width T_0 of the unchirped pulse to get the correct pulse bandwidth, and $L_\mathrm{NL} = 0.26$ m for the input pulse) and we can see that both dispersion and SPM contribute to the pulse evolution. Raman scattering was not included here, for clarity, but it

is otherwise important to do so in the case of short femtosecond pulses for more precise numerical estimates. The behaviour is very different in the cases where the fiber has normal dispersion (or more precisely, when the pulse propagates in the normal dispersive regime of the fiber) and the pulse has the opposite chirp, and in the cases where the pulse is not chirped initially [4]. An initially unchirped Gaussian pulse propagating in the normal dispersive fiber regime will broaden and develop oscillations near its edges, a phenomenon called optical wave breaking [34]. This can be understood from reasoning similar to the one use to explain the behaviour in the example above. Optical wave breaking does not happen in the case of anomalous dispersion with an initially unchirped pulse because e.g. the red-shifted part of the pulse cannot follow up with the pulse tail. However, in anomalous dispersive fiber if the pulse is initially chirped we instead see the behaviour shown in the example.

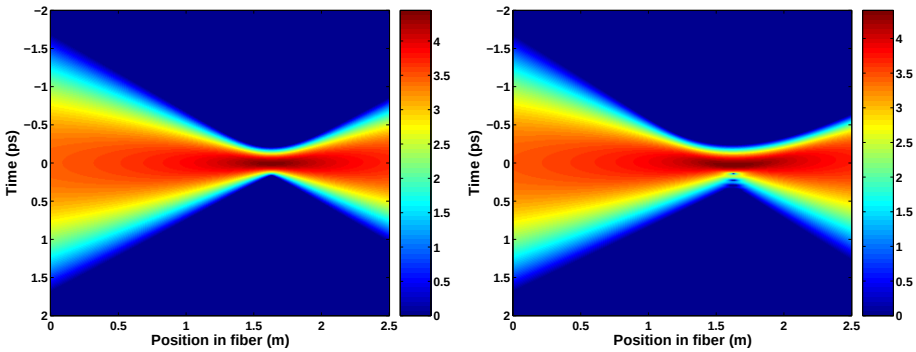

(a)
Fiber parameters:
$\beta_2 = -22\text{ps}^2/\text{km}, \beta_3 = 0\text{ps}^3/\text{km},$
$\gamma = 0\text{W}^{-1}\text{km}^{-1}.$

(b)
Fiber parameters:
$\beta_2 = -22\text{ps}^2/\text{km}, \beta_3 = 0.13\text{ps}^3/\text{km},$
$\gamma = 0\text{W}^{-1}\text{km}^{-1}.$

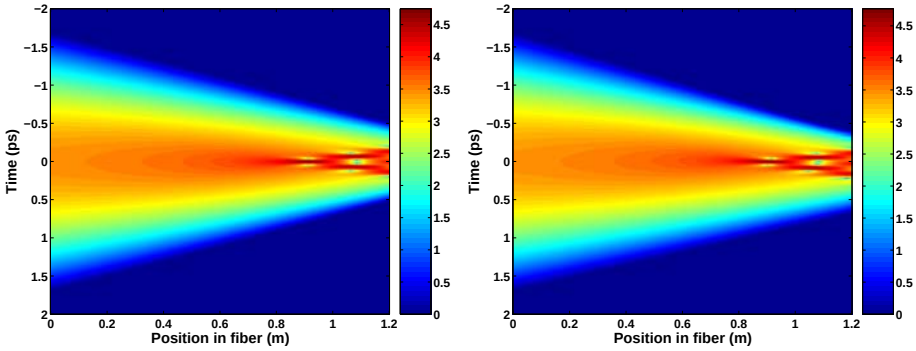

(c)
Fiber parameters:
$\beta_2 = -22\text{ps}^2/\text{km}, \beta_3 = 0\text{ps}^3/\text{km},$
$\gamma = 1.3\text{W}^{-1}\text{km}^{-1}.$

(d)
Fiber parameters:
$\beta_2 = -22\text{ps}^2/\text{km}, \beta_3 = 0.13\text{ps}^3/\text{km},$
$\gamma = 1.3\text{W}^{-1}\text{km}^{-1}.$

Figure 2.2: Propagation of a chirped Gaussian pulse. The plots show the intensity of the pulse as a function of time and as a function of position in the fiber. The intensity scale is in dBW with a threshold value of 1 W.

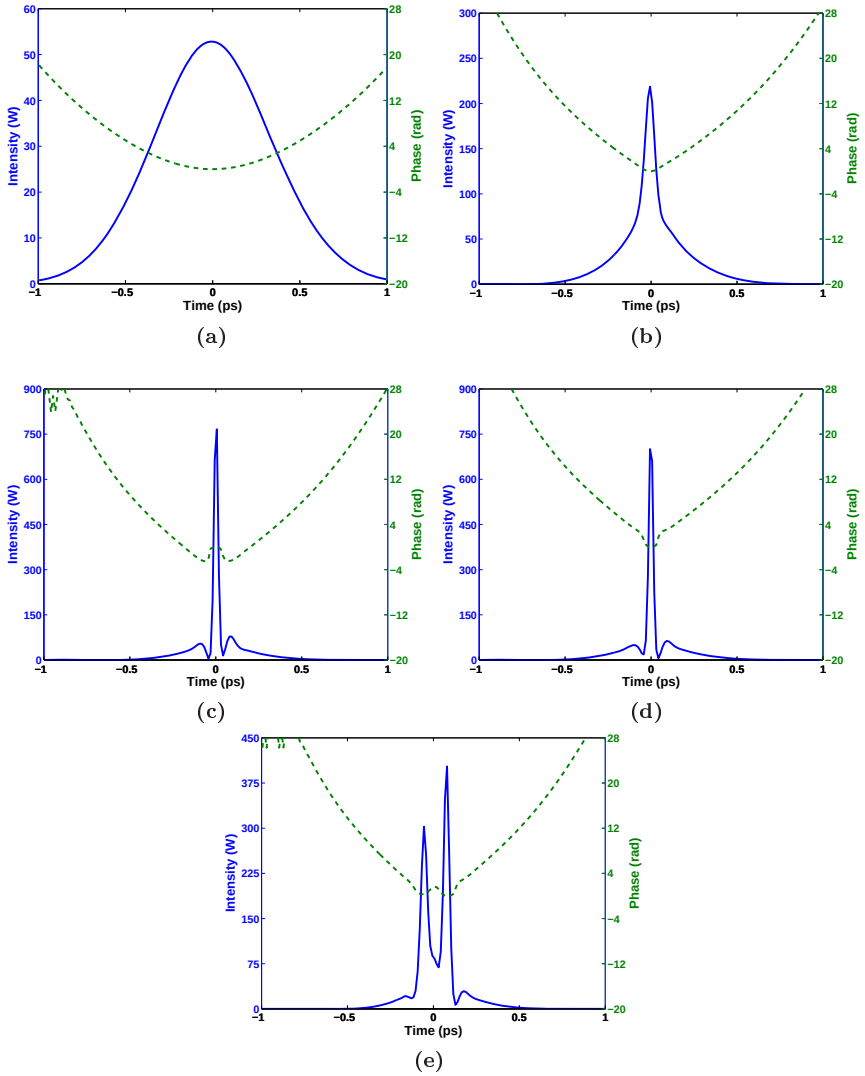

Figure 2.3: A closer look at the pulse intensity (blue, solid line) and phase (green, dashed line) at different positions in the fiber. Plots are at positions 0.30 m (at the beginning of the fiber), 0.80 m (closer to the first compression point), 0.89 m (just before the optimum compression), 0.92 m (at the point where the pulse is compressed), 1.02 m (just before the compression into a double peak). The initial compression occurs faster at the center of the pulse where the intensity is highest. The uneven compression across the pulse is the reason why a significant fraction of the energy resides in the wings of the pulse and not in the main part of the pulse. At the first compression point where the center part of the pulse is compressed there is a phase shift indicating that the chirp in this region changes sign. Then the compression continues but now into two peaks.

CHAPTER 3

Characterization of ultrashort pulses using frequency-resolved optical gating (FROG)

For our experiments we constructed an experimental setup for pulse characterization using second-harmonic generation frequency-resolved optical gating (SHG-FROG). In this chapter we present the measurement setup and the FROG technique.

3.1 Introduction

Frequency-resolved optical gating was introduced in the early 1990s. There are different variants of the FROG technique and they differ in the way the optical gating is implemented [35,36]. An overview can be found in a textbook by Rick Trebino [37]. Frequency-resolved optical gating using second-harmonic generation was demonstrated by Delong *et al.* [38]. One of the advantages of SHG-FROG is a very high sensitivity and pulses with pJ energies can be measured. Typically what is measured is an average of many pulses in a pulse train. Single-shot FROG variants using μJ pulses have been demonstrated as well [39]. A disadvantage of SHG-FROG is time-ambiguity which we describe below.

The techniques available for ultrashort optical pulse measurements are now being used for understanding pulse-shaping mechanisms, spectral broadening processes, soliton dynamics, pulse compression and other phenomena in laser physics and nonlinear optics. Some of the technological challenges today are

measurements of still more complex pulses and measurements of ultrashort optical pulses consisting of only a few optical cycles which implies that the apparatus should be able to measure pulses with very broad bandwidths. A status on the frontiers of ultrashort pulse measurements can be found in reference [40]. The FROG technique has by now been applied to the measurement of very broadband supercontinua generated in photonic crystal fibers [41,42] and it has been used for characterization of pulse propagation in optical fibers [43–45]. Dudley *et al.* gave a detailed characterization of pulse propagation around 1550 nm both in the cases of anomalous and normal dispersion [44, 45].

There has been some discussion in the litterature on ambiguities in FROG measurements because it appeared that two similar yet different pulses resulted in the same FROG spectrograms but this was disputed [46–49]. Practical issues in FROG measurements have been discussed by Delong and coworkers [50].

3.2 The FROG technique

There are no detectors available for direct measurement of picosecond and femtosecond light pulses. To measure such short events it is necessary to make use of another short event. We will describe in the following how a short pulse can be used to measure itself by optical gating in a nonlinear crystal. There are two conventional ways to characterize ultrashort pulses. The first is to measure the optical power spectrum $S(\omega - \omega_0)$. The second is to measure the intensity autocorrelation function which is given by

$$g(\tau) = \int_{-\infty}^{\infty} I(t)I(t-\tau)dt \tag{3.1}$$

It is not possible to deduce the electric field from these two measurements. From the autocorrelation function an estimate of the pulse length can be made assuming that the pulse has a specific shape. Also, considering the spectrum and the autocorrelation in combination it is possible to see if a pulse is stretched in time because of chirp and the amount of chirp can be estimated assuming for example that the chirp is linear.

An illustration of a SHG-FROG setup is shown in figure 3.1. The SHG signal is given by

$$E_{\text{sig}}(t,\tau) = E(t)E(t-\tau), \tag{3.2}$$

and the spectrum recorded by the spectrometer is

$$I_{\text{FROG}}(\omega,\tau) = \left| \int_{-\infty}^{\infty} E_{\text{sig}}(t,\tau)e^{-i\omega t}dt \right|^2 \tag{3.3}$$

These time and frequency data are the *spectrogram* of the pulse. The spectrogram contains all information about the pulse and it gives a graphical repre-

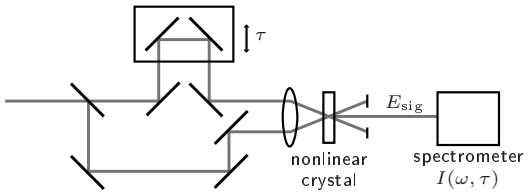

Figure 3.1: SHG-FROG measurement scheme.

sentation on the pulse. The electric field can be retrieved from the spectrogram in an iterative *phase retrieval* process.
If the spectrogram is integrated along the frequency variable we get the *delay marginal*

$$M_\tau(\tau) = \int_{-\infty}^{\infty} I_{\mathrm{FROG}}(\omega, \tau) d\omega, \tag{3.4}$$

In the case of SHG-FROG the delay marginal is identical to the standard intensity autocorrelation function

$$M_\tau^{\mathrm{SHG}}(\tau) = \int_{-\infty}^{\infty} I(t) I(t-\tau) dt \tag{3.5}$$

The spectrogram can also be integrated along the delay variable and we get the *frequency marginal*

$$M_\omega(\omega) = \int_{-\infty}^{\infty} I_{\mathrm{FROG}}(\omega, \tau) d\tau \tag{3.6}$$

In the case of SHG-FROG the frequency marginal should have the same functional form as the autoconvolution of the pulse spectrum

$$M_\omega^{\mathrm{SHG}}(\omega - 2\omega_0) = S(\omega - \omega 0) * S(\omega - \omega 0) \tag{3.7}$$

The delay and frequency marginals are useful for checking the consistency of the measurements. If the frequency marginal does not satisfy the relation to the original pulse spectrum then there are one or more systematic errors in the measurements. This could be due to nonuniform phasematching in the nonlinear crystal, calibration errors in the spectrometer or some spectral filtering in the optics. The frequency marginal can also be used to compensate for nonuniform phasematching such that eq. 3.6 is satisfied. An example is shown in figure 3.2. In the case of SHG-FROG the delay marginal should be identical to an indepently measured autocorrelation.

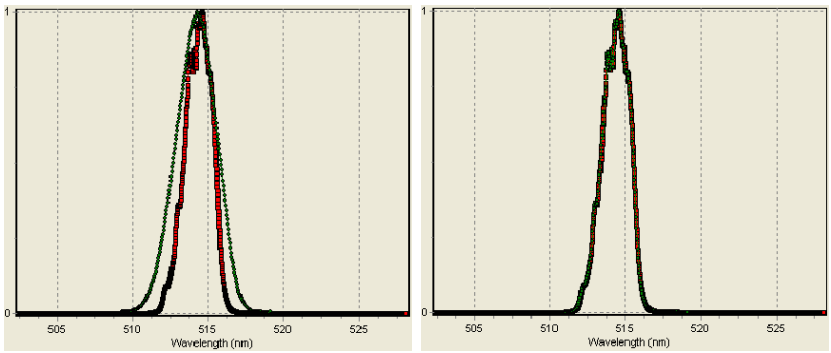

Figure 3.2: Example of a marginal errors in FROG measurements (left) which leads to an adjustment of the spectrogram to the frequency marginal (right). The example shows results for a picosecond pulse with center wavelength at 1028 nm. The figures show the marginal from the FROG data (green circles) and the frequency marginal (red squares).

3.3 Measurement setup

The FROG measurement setup that we have constructed is shown in figure 3.3. The input pulse is split on a beam splitter into a *signal* pulse and a *gating* pulse. The gating pulse is shifted in time with respect to the signal pulse using an optical delay line. The delay line consists of a retro reflector positioned on a motorized translation stage (Newport, M-ILS250) with a 25 cm scanning range. The translation stage is controlled by LabVIEW software. The change in time delay τ is 6.7 fs for each μm the translation stage moves because of the change in optical path length. The signal pulse and the gating pulse are focused in the nonlinear crystal where they overlap spatially. The SFG signal from the crystal is detected using a grating spectrometer (Ocean Optics, HR2000+) with a 0.46 nm resolution. The spectrometer is also controlled by the LabVIEW software. The spectrum of the input pulse is measured with an optical spectrum analyzer (OSA).

The setup is also used for XFROG measurements. In this case the fiber under test is inserted in the signal arm of setup together with coupling lenses and an extra delay line is inserted in the gating arm of the setup such that the optical path lengths in the two arms are equal, or, more precisely, such that the motorized translation stage can be moved to make the path lengths equal. Another option is to remove the input beam splitter and instead make cross-correlation measurements of the input beam and a secondary input beam. We have used this for cross-correlation measurements of two synchronized fiber lasers.

We use BBO (β-Barium Borate, BaB_2O_4) crystals with thicknesses of 40 μm and 130 μm cut for second-harmonic generation of 1030 nm and 1550 nm respectively. The crystals are from Castech Inc. They are cut for type I phasematching and have P-coating (protective coating). Phasematching over tens of nanometers can be achived with such thin nonlinear crystals and it can be shown that the SHG response is reasonably uniform over a few nanometers for a 1 mm thick crystal and that it is uniform over tens of nanometers for a 100 μm thick crystal [44].

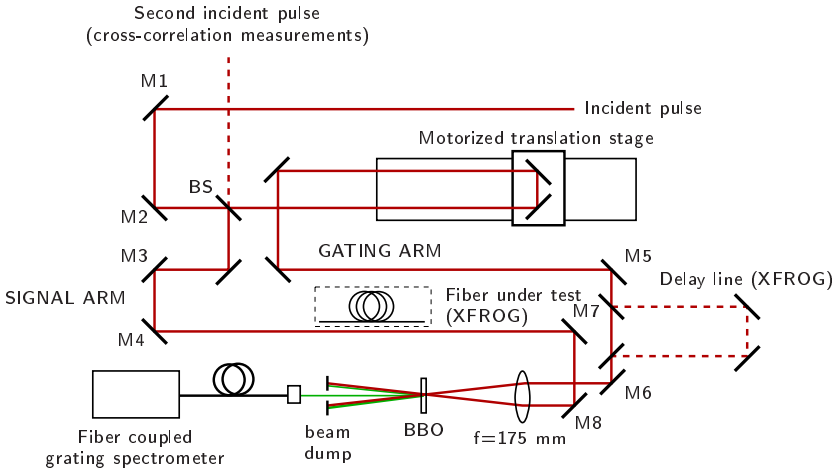

Figure 3.3: Measurement setup (BS - beam splitter, M1-M8 mirrors). When the setup is used for XFROG measurement the fiber under test is inserted in the signal arm and an extra delay line is inserted in the gating arm. The SFG signal is picked up by a fiber going into the grating spectrometer. The two fundamental beams and the accompanying SHG signals are blocked after the crystal (beam dump). If the signal beam and the gating beam are collimated and parallel when they enter the focusing lense (focal length, f=175 mm) then the focus point and the overlap point coincides.

Phase retrieval

The pulse intensity and phase can be retrieved from the FROG spectrogram in an iterative phase retrieval procedure. We used the software Frog3 from Femtosoft Technologies [51] for phase retrievel. The many spectrograms presented in chapter 5 were retrieved using Matlab with a DLL library compiled from Frog3 source code, courtesy of Femtosoft Technologies. It is straightforward to implement a fast retrieval algorithm known as principal components generalized projections (PCGP) in Matlab [52]. We did this and found that the

retrieval results were similar to the ones of the commercial software but the commercial programs are compiled and are faster. They also try other strategies for retrieval if the retrieval starts to stagger. Very fast retrieval algoritms based on PCGP can be used for real-time measurements [53]. This is described in detail in a review paper by Daniel Kane [54].

Time ambiguity

The SHG-FROG spectrogram is symmetric in time, that is, $E(t)$ and $E(-t)$ will result in the same spectrogram. It is therefore not possible to tell from the spectrogram if a pulse moves forward or backward on the time axis. In practice this is not a problem. We often have some prior knowledge about the pulse that is measured, e.g. that this pulse gets compressed if it propagates in silica glass, and this then tells us the sign of the chirp and thereby the direction of the pulse in time. Other FROG geometries do not have this time-ambiguity and the spectrograms are more intuitive and easier to interpret.

FROG sampling rate

On a FROG trace with $N \times N$ points the delay step size is

$$\Delta t = T/N, \tag{3.8}$$

where T is the size of the time window. The retrieval algoritms make use of the fast Fourier transform and from the Fourier transform the frequency step is

$$\Delta f = \frac{1}{N\Delta t} \tag{3.9}$$

and the size of the frequency window W is then

$$W = N\Delta f = \frac{1}{\Delta t} \tag{3.10}$$

This determines the sampling grid. The FROG spectrogram is properly sampled when data are not truncated, that is, the FROG signal should lie within the sampling grid. In practice a signal can be considered properly sampled when all data points with a higher intensity than 10^{-4} of the maximum value are within the sampling grid [50]. Looking for a suitable sampling grid we first choose Δt so small that the frequency window W is large enough. Then we select a grid size $N \times N$ such that the time window gets large enough. A larger grid size will make the retrievel algoritme slower.

Experimental considerations - aligning the setup

Aligning the measurement setup we want to be certain that what we measure is the actual pulse. The frequency marginal should look like the SHG spectrum

that is expected from measurements of the spectrum of the input pulse (cf. eq. 3.6). If it does not it could be because of nonuniform phasematching in the nonlinear crystal due to the orientation of the nonlinear crystal, or because of an error in the spectrometer itself. Specifically for SHG-FROG the spectrogram should be symmetric in time. If this is not the case the delay translation stage is most likely misaligned. Retrieving pulses from a measured spectrogram we make sure that there is good agreement between the measured spectrogram and the spectrogram of the retrieved pulse. Basically, they should look alike. Even for reasonably low FROG errors around $2-3\%$ there is a chance that something has gone wrong in the retrieval. We can of course also check if the retrieved pulse shape and phase is what we would expect.

CHAPTER 4

Modelocked femtosecond fiber laser at 1028 nm

In this chapter we present an effective solution for an all-polarization maintaining (PM) modelocked femtosecond fiber laser operating at the central wavelength of 1028 nm. The laser is based on an ytterbium(Yb)-doped active fiber. Modelocking is enabled by a semiconductor saturable absorber mirror, and the central wavelength is enforced by a fiber Bragg grating. The laser is self-starting and demonstrates excellent stability against Q-switching. The pulse repetition rate of the oscillator was 31 MHz. The repetition rate was reduced by pulse picking and the output was further amplified in PM Yb fiber amplifiers to increase the pulse energy. Amplified pulses had pulse energies up to more than 130 nJ at a repetition rate of 488 kHz. In chapter 6 we present results on dispersive compression of the laser pulses in a hollow-core photonic fiber with anomalous dispersion at 1028 nm.

We used another version of this laser system in our initial experiments. The laser system featured the same oscillator but the cavity length was longer such that the pulse repetition rate was 34 MHz. The output of the oscillator was amplified directly in a PM fiber amplifier to a pulse energy of 13 nJ. The pulses were spectrally broadened in single-mode fiber and external compression lead to near transform-limited pulses of 140 fs. The results are discussion in section 4.3. We reported on this fiber laser in reference [55].

In the following sections we describe the laser oscillator, the fiber amplifiers and the optical pulse picking in turn.

4.1 Introduction

In the recent years an impressive progress was achieved in development of femtosecond fibers lasers. State of the art femtosecond fiber lasers compete successfully with solid-state femtosecond oscillators in both pulse duration and output power. Utilizing an existing fiber technology in construction of a laser enables one to achieve the slope efficiencies as high as 60-80%, to drastically reduce the device cost, and to significantly simplify the manufacturing process. However, most of the demonstrated fiber lasers are not monolithic, i.e. free-space coupling of light in and out of active and/or passive laser components is often used [56–58]. Such free-space coupling, especially when used inside the laser cavity, makes the laser susceptible to mechanical instabilities, and thus limits the areas of use of such lasers. For the applications such as defence, homeland security, medicine etc., a cheap, compact, self-starting femtosecond lasers are needed, that are mechanically stable and do not require personnel with specialized training to operate.

4.2 Overview of the fiber laser system

Our laser system consists of five stages: a modelocked picosecond oscillator, a pre-amplifier, a free-space pulse picker, and two additional fiber amplifiers. All fibers used in the laser are single-mode (SM) and polarization-maintaining (PM). All parts, except for the free-space pulse picker, are spliced together. The layout of the laser is shown in figure 4.1.

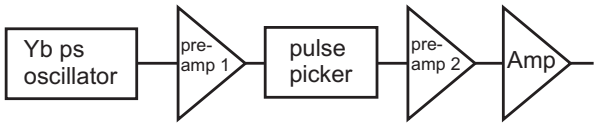

Figure 4.1: The layout of the fiber laser.

The power budget is shown in table 4.1 below. In the power budget we assume that the maximum output power of the first pre-amplifier is 100 mW, in practice up to 120 mW was available. The power transmission of the pulse picker when all pulses are transmitted is approximately 50% including the coupling loss to the second fiber amplifier. It is estimated that the power gain is 12 dB in the second amplifier and 10 dB in the last amplifier. Approximately 40% of the power was lost in a Faraday isolator (not shown in the layout) between the two amplifiers. The design of all three amplifiers was the same except that the second pre-amplifier was optically pumped in both the forward direction and in the backward direction which is the reason for the higher gain in that

amplifier. The pulses were stretched additionally in 3 m single-mode fiber after the first pre-amplifier to a few picoseconds pulse duration. This was done to lower the peak power in the next amplifiers in order to reduce nonlinear effects.

	P_{avr} (mW)	f_{rep} (MHz)	E_{pulse} (nJ)
Output of pre-amplifier 1	100	31.2	3.2
Output of the pulse picker	0.78	0.488	1.6
Output of pre-amplifier 2	12.36	0.488	25.4
Output of isolator	7.4	0.488	15.2
Output of final amplifier	74	0.488	152

Table 4.1: Power budget. Average power P_{avr}, pulse repetition rate f_{rep} and pulse energy E_{pulse} at different stages of the laser system when the repetition rate is reduced by a factor of 64 to 488 kHz.

Fiber oscillator

The oscillator is a linear cavity laser with a resonator length of approximately 3 m, of which 0.5 m is active Yb-doped fiber. This length provides the repetition rate of 31 MHz. The cavity is confined between a fiber Bragg grating with a stop-band centered at 1028 nm, and a butt-coupled semiconductor saturable absorber mirror (SESAM) with a saturable loss of 24%. The oscillator is pumped by a laser diode operating at 976 nm through a 980/1064 wavelength division multiplexer (WDM). The outcoupling is performed via a 20% - off polarization filter coupler (PFC) into two tap ports. One tap port is used as a monitor, and another one is directed into the amplifier stage via a polarization-maintaining unidirectional isolator (PISO). The isolator protects the oscillator from reflections from the pre-amplifiers. The oscillator has a lasing threshold of 55 mW, and demonstrates modelocking of excellent stability in the pumping

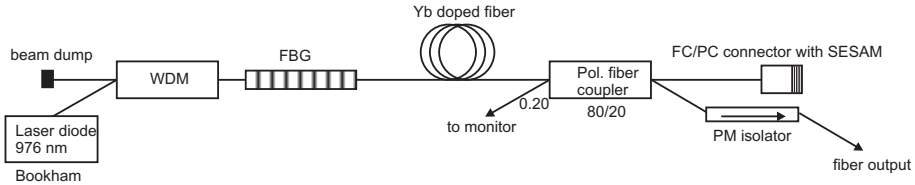

Figure 4.2: The fiber oscillator.

range 55 − 65 mW. At higher pump powers the laser tends to enter the Q-switch modelocking regime. The oscillator seed signal has an average power of 1.3 mW, which at the repetition rate of 31 MHz corresponds to a pulse energy of approximately 40 pJ.

First pre-amplifier (PA1)

The oscillator signal is amplified in the first pre-amplifier PA1 to around 120 mW. The amplifier consists of a piece of PM Yb-doped fiber and a WDM for coupling the signal and the pump light into the active fiber. The gain saturates at higher pump powers. This is seen in figure 4.3 which shows the output power for different pump powers and figures 4.4 and 4.5 which show the spectra for different powers. The output power is limited by the amount of seed signal and not by the pump power which can be more than 300 mW. The increasing spectral broadening with power, due to SPM, is clearly seen.

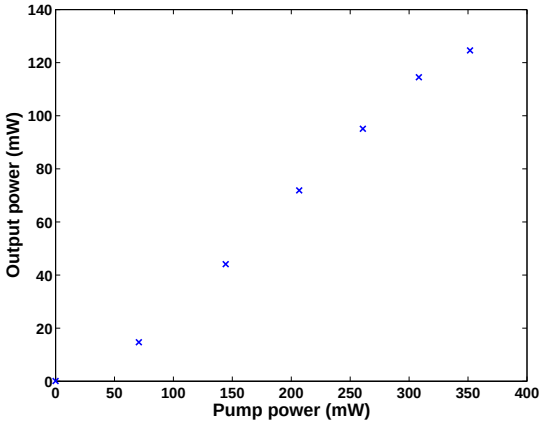

Figure 4.3: The output power from the first pre-amplifier PA1 as a function of pump power.

Pulse picker

The purpose of the pulse picker is to reduce the repetition rate of the optical pulses. The pulse picker electronics is described in appendix A. The electronics triggers on a signal from a fast pulse detector that monitors the pulse train. It counts the number of pulses and after a certain number of pulses it sends out a nanosecond pulse that is input to an rf driver connected to an acousto-optic modulator (AOM). When the AOM crystal is modulated a fraction of the

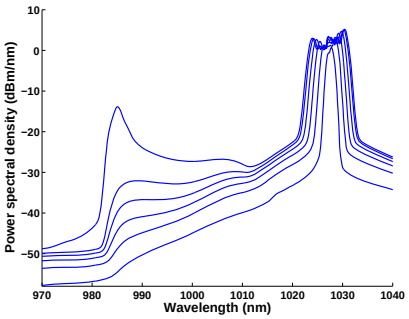

Figure 4.4: Spectra of the output from the first pre-amplifier PA1 for output powers from 14 mW to 122 mW (logarithmic scale).

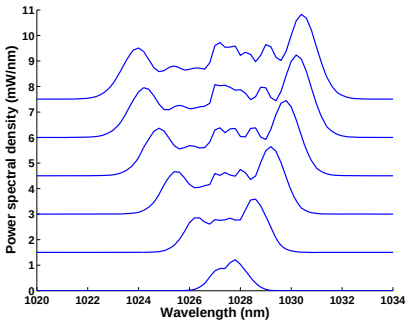

Figure 4.5: Same spectra as in figure 4.4 but only showing the signal light around 1028 nm (linear scale).

light is diffracted and coupled into the second pre-amplifier using an aspheric lense. The repetition rates that were available in our system after pulse picking were 31.3 MHz (the frequency of the fiber oscillator itself), 7.8 MHz, 3.9 MHz, 1.96 MHz, 977.8 kHz, 488.9 kHz, 244.5 kHz and 122.2 kHz. The highest pulse energies for this laser system was achived with a repetition rate of 488.9 kHz.

An example is shown in figure 4.6 where the repetition rate of the pulse train is reduced from 31.3 MHz to 7.8 MHz. The duration of the rf pulse is typically chosen to be a little less than the period of the optical pulse train. The purpose is to let one and only one pulse through. The rise and fall time of the rf modulation is determined by the characteristics of the trigger electronics and by the time that it takes the rf modulation to pass the AOM crystal. If the rf pulse is too long then more than one optical pulse will pass through the pulse picker (see figure 4.7). On the other hand there is a limit to how short the trigger pulse can be because of the finite rise and fall time. Here we have used a 0.1 mm crystal and typical rise and fall times are approximately 10 ns.

Pulse amplification after pulse picking

The pulses were further amplified in two amplifier stages. The design was similar to the design of the first pre-amplifier with approximately 1.2 m yb-doped fiber in each. The first of these two amplifiers (PA2) was pumped in both the forward and the backwards direction to achive a more uniform and overall higher gain. The output power of PA2 as a function of pump power for different repetition rates is shown in figure 4.8. The average power is lower at lower repetition rates. However, the amplifier gain is higher at lower repetition

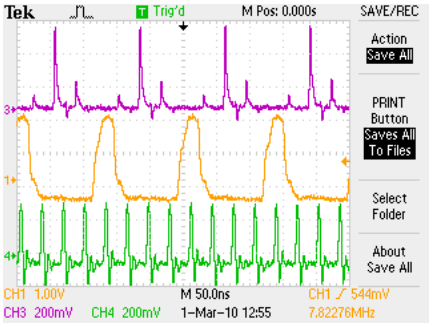

Figure 4.6: Oscilloscope signals showing the pulse train from the oscillator (green, bottom curve) measured with a Si amplified detector (Thorlabs, PDA10A-EC), the electronic signal that triggers the rf modulation (orange, middle curve) and the output of the pulse picker (purple, top curve) measured with a InGaAs biased detector (Thorlabs, Det10C).

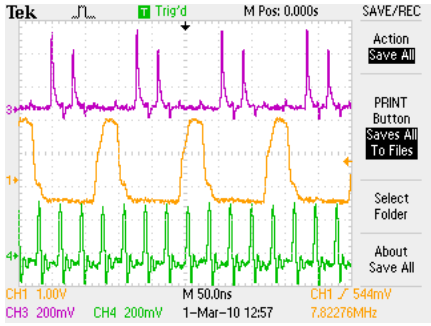

Figure 4.7: Same oscilloscope signals as in figure 4.6 but with the electronic trigger signal shifted slightly with respect to the optical pulse train. In this case more of the second, trailing pulse is transmitted. We can avoid this by using a short trigger pulse and by finding a suitable setting for the trigger delay.

rates such that the energy per pulse is higher. The PA2 output spectra are shown in figure 4.2. In the low repetition rate case increasing amplified spontaneous emission (ASE) can be seen in the spectra at higher pump powers. With the final amplifier the signal was amplified to around 80 mW at 489 kHz corresponding to pulse energies of approximately 164 nJ. The spectra of the output pulses are shown in figure 4.10 for different pump powers. The length of yb-doped fiber in the last amplifier was made short to minimize self-phase modulation and stimulated Raman scattering. An FC/APC-connector was spliced onto the output of the yb fiber to avoid back reflections from the fiber output facet.

4.3 Spectral broadening and pulse compression

We investigated spectral broadening and compression of the optical pulses with another version of the fiber laser. This version of the laser did not make use of the pulse picker and instead the oscillator output went directly into a fiber amplifier. The optical pulses were spectrally broadened in standard single-mode PM fiber (PM980 panda fiber) and pulse compression of the optical pulses was done in a free-space grating compressor at the end of the system.

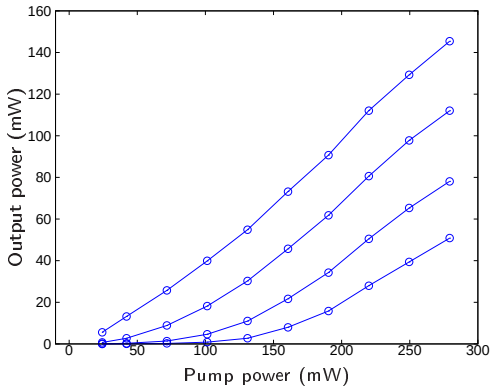

Figure 4.8: PA2 output power as a function of pump power for different repetition rates (the circles are the measurements and the lines are there to guide the eye). From the top: 31.29 MHz (with continuous rf modulation in the pulse picker and all pulses transmitted), 7.82 MHz, 978 kHz and 122 kHz.

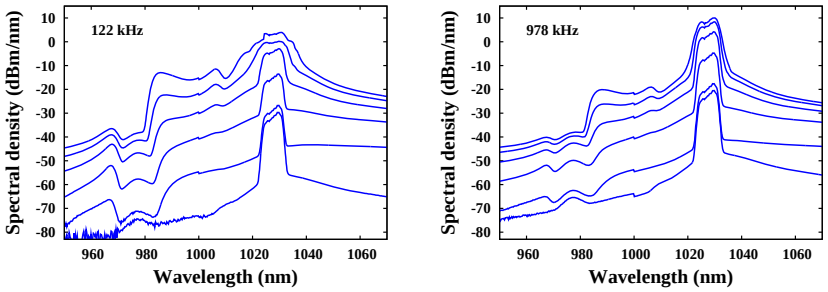

Figure 4.9: PA2 output spectra (logarithmic scale) for two different repetition rates for pump powers 0 mW, 14 mW, 72 mW, 131 mW, 191 mW and 250 mW.

The amplifier stage consists of 2 m of active Yb-doped fiber, pumped by another 976 nm laser diode via a WDM. The oscillator signal is sent to the seed port of this WDM. The amplified laser signal is sent through approximately 10 m of single-mode PM fiber, where the significant spectrum broadening is achieved due to self-phase modulation. The spectrum from the oscillator and the spectrum of the pulse after spectral broadening are compared in figure 4.11. Amplification of the seed signal in the pump power range $0 - 625$ mW shows a linear dependency of the laser output power on the amplifier input pump

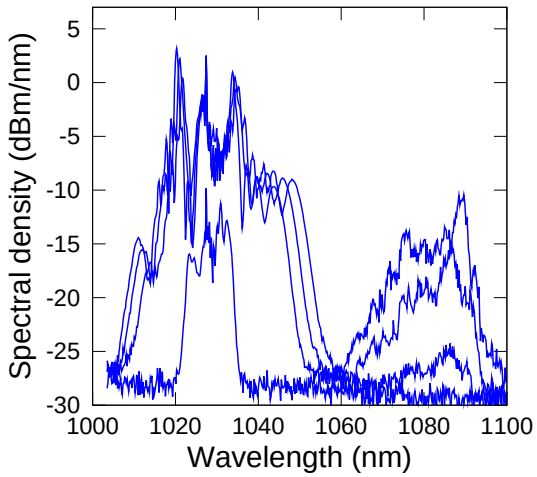

Figure 4.10: The third amplifier output spectra (logarithmic scale) at a repetition rate of 489 kHz with average output powers of 2 mW, 39 mW (corresponding to a pulse energy of 81 nJ), 53 mW (109 nJ) and 63 mW (128 nJ).

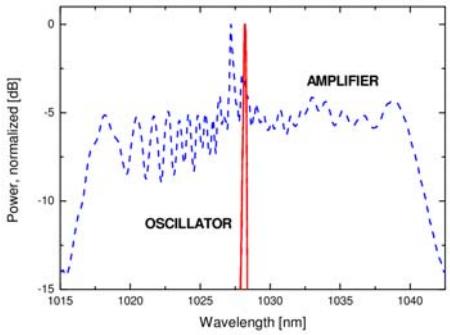

Figure 4.11: Normalized power spectra of the oscillator (red, solid line) and the amplifier (blue, dashed line). Oscillator spectrum was measured after the isolator, and the amplifier spectrum was measured after the spectral-broadening single-mode fiber. Pump powers for the oscillator and the amplifier were 55 mW and 625 mW, respectively.

power with a slope efficiency of 70%, and leads to the highest generated output

power of 440 mW, as shown in figure 4.12. Given the repetition rate, we thus were able to produce the laser pulses with the pulse energy reaching 13 nJ. We note here that there is no sign of gain saturation in the amplifier, and thus the highest generated output power is only limited by the highest possible pump power of our laser diode, which was 625 mW.

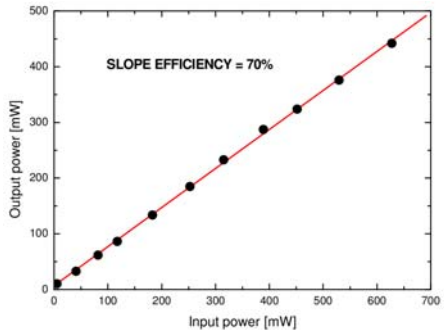

Figure 4.12: Dependency of the amplifier output power on the input pump power.

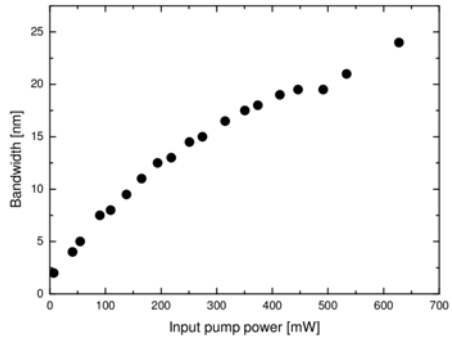

Figure 4.13: Dependency of the amplifier output spectrum bandwidth on the input pump power.

As described above, the amplified laser signal is spectrally broadened in a single-mode fiber due to self-phase modulation. In figure 4.13 the dependency of generated spectral bandwidth on the input pump power of the amplifier is shown. The spectral bandwidth grows monotonically with input pump power, and shows saturating behavior. At the highest possible pump power of 625

mW the generated spectral bandwidth reached 24 nm, which in this wavelength range corresponds to 6 THz. Both the amplification and the spectral broadening dynamics of the laser suggest that using a stronger amplifier pump laser diode would result in considerable further amplification and spectral bandwidth generation.

The laser output is collimated and sent through a grating compressor. The resulting ultrashort pulses were characterized using a noncollinear scanning autocorrelator and a GRENOUILLE setup (see figure4.14) [37]. The grating compressor has a power transmission coefficient of 72%. Before compression the autocorrelation of the pulses was approximately 7 ps at FWHM. Both the autocorrelation and the GRENOUILLE measurements of the shortest compressed pulses show pulse shapes with pronounced side wings of the pulse. We attribute this to the complexity of the spectrum, generated in the long single-mode fiber. Slightly asymmetric shape of the GRENOUILLE trace was persistent over the full range of grating separation distances in the compressor, and demonstrates a moderate share of higher-order chirp in the pulse, which was supported by the phase information retrieved by the GRENOUILLE (not shown here). Such higher-order chirp is the natural consequence of self-phase modulation in the single-mode fiber. The full width at half maximum (FWHM) of the autocorrelation signal was measured to be of 175 fs, which implies that the deconvoluted pulse duration at FWHM is less than that [59]. The FWHM of the GRENOUILLE signal was measured to be of 140 fs. Given the output spectral bandwidth of 6 THz, we can conclude that the resulted laser pulses are near transform-limited. The analysis of GRENOUILLE trace shows that 73% of the intensity of the laser pulse belongs to its main peak and lies within $\pm$120 fs boundaries.

4.4 Discussion and conclusion

In conclusion, we have presented a linear cavity, all-polarization-maintaining picosecond laser based on Yb-doped active fiber as a gain medium. The laser is self-starting and demonstrates excellent modelocking stability in a wide oscillator pump range. The first version of laser had a repetition rate of 34 MHz, and maximum output power of 440 mW, which corresponds to a pulse energy of 13 nJ. The pulses could be compressed to femtosecond pulses in a free-space-coupled grating based compressor at the end of the system. Amplification and spectral broadening dynamics shows high potential for generating stronger and shorter pulses using this laser design. The second version of the laser featured pulse picking and further amplification which resulted in pulse energies at the 100 nJ level. Higher pulse energies would be interesting for a number of applications, e.g. high-power supercontinuum generation or research in soliton excitation in hollow-core fiber. One possible way to proceed is to splice the

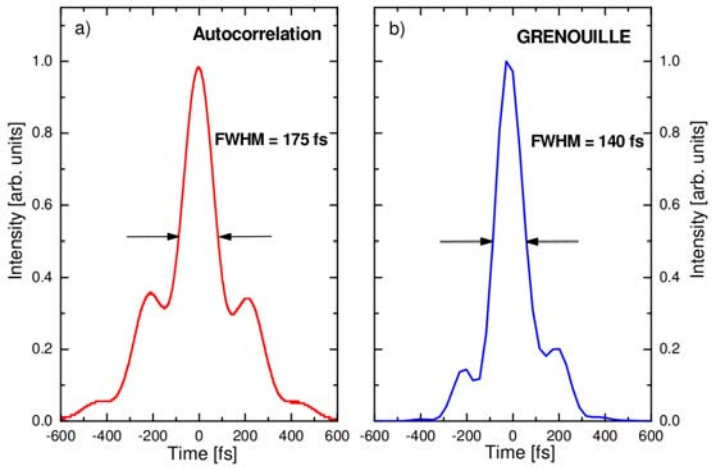

Figure 4.14: Noncollinear intensity autocorrelation (a) and GRENOUILLE measurement (b) of the shortest compressed laser pulse. The amplifier pump power was 625 mW.

output of the fiber laser to a cladding pumped fiber amplifier module.

CHAPTER 5

Fiber links for nJ femtosecond laser pulses at 1550 nm with applications in terahertz imaging

In this chapter we present results for two different optical fiber links that were developed for transmission of nJ femtosecond laser pulses at 1550 nm. The fiber links were originally intended for applications in terahertz imaging systems and for use in terahertz time-domain spectroscopy systems. The main result in this chapter is a numerical and experimental characterization of the performance of the fiber links.

The first fiber link that is presented here is a single channel link. The link consist of dispersion-compensating fiber (DCF) and standard single-mode fiber. It was optimized for the delivery of sub-100-fs laser pulses at 1550 nm over several meters of fiber. We were interested in the power handling capacity of the fiber link and all-fiber delivery of 1-nJ pulses over a distance of 5.3 m was demonstrated. The optical pulses at different positions in the fiber link were measured using frequency-resolved optical gating (FROG). The results are compared with numerical simulations of the pulse propagation based on the generalized nonlinear Schrödinger equation.

The second fiber link is a multi-channel link. The basic design is similar to the design of the single channel link but now the input pulse is being split into multiple pulses and distributed in multiple fibers. This allows a higher input pulse energy in the initial part of the fiber link before the pulse is split into the different channels. This higher input power capacity of the fiber link allows the distribution of femtosecond pulses to an array of fibers which has applications in multi-channel fiber-coupled terahertz imaging systems. As an

example we have demonstrated THz pulse generation and detection using a distributed fiber link with 32 channels and 2.6 nJ input pulse energy. The results mentioned above were published in reference [60].

At the end of the chapter we discuss the experimental methods in greater detail and we present additional results on the fiber links. We discuss some of the limitations in this type of fiber links and we consider the quality of the compressed pulses. We show that the transmission of 1.2 nJ pulses in the single-channel fiber link results in pulses with poor pulse quality. This is also expected from numerical simulations.

5.1 Overview

Delivery of nJ, sub-100-fs laser pulses via an all-fiber distribution link has many applications in multi-photon microscopy [8], terahertz spectroscopy [9] and terahertz imaging [10] as well as in other areas where beam delivery of fs-pulses via optical fiber is of an advantage. All-fiber pulse compression schemes are also of interest for fiber amplifier systems where it can replace bulk optics prism or grating compressors.

Dispersion management of sub-100-fs pulses in the linear regime using dispersion-compensating fiber (DCF) at 1300 nm to 1700 nm wavelength has originally been proposed by Lin et al. [12] and was treated in a review of DCF fibers by Grüner-Nielsen et al. [11]. Chang et al. [13] demonstrated nearly dispersion-free transmission of sub-100-fs pulses in the low picojoule energy range over a 42 m concatenated single-mode fiber (SMF) - DCF fiber link. In this and similar dispersion compensation experiments the idea is to match the dispersion of the SMF with the dispersion of a piece of DCF that has the same magnitude but is opposite in sign. For very short pulses or long fiber lengths the third-order dispersion (TOD) has to be efficiently compensated as well. Since the pulse peak power in these experiments was low, nonlinear effects were negligible.

Pulse delivery of nanojoule femtosecond pulses through large-mode-area (LMA) fibers has been demonstrated by Ouzounov et al. [14]. Here 3 nJ pre-chirped input pulses were compressed to 140 fs, and it was demonstrated that LMA fiber under the same conditions delivered 10 times shorter pulses than standard SMF due to reduced self-phase modulation (SPM).

Propagation in standard and dispersion-shifted fibers around 1550 nm has been studied experimentally using frequency-resolved optical gating (FROG) [44]. The FROG technique allows a detailed characterization of higher-order soliton evolution and pulse propagation near the zero dispersion wavelength of an optical fiber.

Recent work on pulse delivery of sub-100-fs, < 800 nm pulses with micro-joule pulse energies in specialty hollow core PCF has been demonstrated by

Skibina et al. [15]. The chirped HC-PCF fiber showed very low dispersion enabling delivery of pulses with duration as short as 26 fs through 1 m fiber, without further dispersion management.

Terahertz time-domain spectroscopy (THz-TDS) and THz-imaging using photoconductive switches are two areas within the terahertz field with an increasing amount of emerging applications [9, 10]. One limiting factor on the application side is the complexity of the free-space optical systems requiring ultrafast lasers pulses ($<$ 100 fs) to pump and probe the THz emitters and detectors, respectively. The field has advanced with respect to robustness and applicability with the advent of more simple fiber-pigtailed measuring setups using movable fiber-coupled emitters and detectors. Rudd et al. [61] avoided first free-space optics in their fiber-pigtailed THz sensor heads by pre-chirping the ultrafast laser pulses in an external grating compressor prior to fiber-launch. An existing commercial version is the Picometrix T-Ray 4000 TD-THz System [62].

Sartorius et al. recently demonstrated an all-fiber THz-TDS system using low-temperature-grown InGaAs/InAlAs multi-layer photoconductive switches [63]. In this system, a pulsed fiber laser operating at 1550 nm delivered 100-fs, sub-nJ pulses which were precompensated inside the laser unit for 10 m single-mode fiber.

Another application of a fiber based distribution link is that it enables multi-channel THz systems by using fiber splitters to distribute the pulses throughout the network. The sub-100-fs pulses are then fed into an array of individual photoconductive switches which generate or detect THz radiation [64].

Here we explore all-fiber dispersion management for the 1.55-μm wavelength range, with special emphasis on the transition from low-power propagation where standard dispersive effects determine the final pulse duration, to high-power propagation where nonlinear effects and, in particular, SPM become decisive for the pulse quality at the output of the fiber link. We demonstrate transmission of pulses at 1 nJ energy which are compressed to sub-100 fs duration. We observe that SPM has a significant effect of the compression. In our experiments the input pulse is the positively chirped output from an amplified Er-doped fiber laser. We initially stretch the pulse further in DCF fiber and then compress it to its final duration in several meters of standard single-mode fiber. The fiber link is characterized by measuring the pulses at different positions in the fiber link in a cutback experiment and using second-harmonic frequency resolved optical gating (SHG-FROG) for pulse measurements [38]. Finally we demonstrate that by increasing the input energy to 2.6 nJ and splitting the fiber link into 32 channels, the link can be an important component for distribution of femtosecond laser pulses to arrays of THz antennas.

The advantages of the approach presented here for the 1.55-μm wavelength range are the straight forward low-loss fusion splicing techniques for telecom

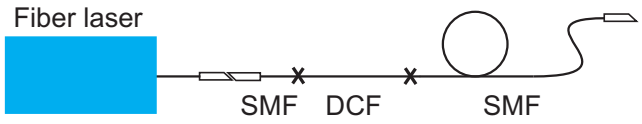

Figure 5.1: Fiber link design. The output of the fiber laser is butt-coupled to the fiber link using FC/APC connectors. The crosses show where SMF and DCF fiber sections are spliced together.

fibers, and the availability of low-cost of-the-shelf fibers and standard components such as isolators and power splitters.

5.2 Fiber link design

The fiber link is designed to deliver nJ sub-100 fs pulses after a few meters of optical fiber (see figure 5.1). The link consist of 0.56 m EWB DCF (extra-wide-band DCF) [11] which is pigtailed with 20 cm SMF at each end and then spliced onto approximately 5 m of standard SMF. The DCF is a standard component in dispersion-managed cables in low-power telecom applications. The DCF has a high dispersion parameter D and a high nonlinear coefficient γ because of a small mode area. The dispersion of the DCF fiber is normal at 1550 nm, with a relative dispersion slope (RDS) precisely matched to that of standard SMF. The fiber parameters are summarized in table 5.1. The splice loss for each of the two splices between SMF and DCF is 0.3 dB. A FC/APC connector is spliced onto the input fiber such that the total length of SMF fiber before the DCF fiber is 37.5 cm. The optimum length of the final SMF fiber in the fiber link will depend on the energy of the pulse. The optimum length for our purposes is determined in fiber cutback measurements and the results are shown below.

After the first small piece of SMF fiber, the positively chirped input pulse is further stretched in the DCF fiber section. This increases the total length of the fiber link from approximately 0.7 m without additional DCF to more than 5 m with 0.56 m of DCF. The additional stretching of the pulse after the DCF section also offers a point in the fiber link with relatively low peak power of the pulse. At this point, additional fiber elements with limited peak power capability can be inserted with the lowest risk of optical damage. In the last section of the paper we will demonstrate this by inserting a 1x32 power splitter based on planar glass waveguide technology in the fiber link. After the DCF section the pulse is compressed to its shortest duration in standard single-mode fiber due to a combination of anomalous dispersion and SPM [4].

5.3 Characterization of the fiber laser input

The femtosecond light source that is used in the experiments is an FFS.SYS mode-locked 1550 nm fiber laser from TOPTICA Photonics AG. The system was originally designed to deliver 100 fs pulses into free space with an average power of 250 mW. We removed the free-space prism compressor inside the laser and replaced it by an FC/APC connector spliced directly on the output of the amplifier section of the fiber laser. The fiber laser output, i.e. the input to the fiber link, was characterized by FROG after the FC/APC connector as shown in figure 5.2. The FROG retrieval errors were typically on the order of 1-3% for this and all other FROG traces reported here, with 256^2 points in the FROG spectrogram. The phase of the input pulse is nearly quadratic with a negative curvature, which shows that it has a linear and positive chirp. The input pulse has a full-width-at-half-maximum (FWHM) duration of 0.8 ps and a center wavelength around 1550 nm.

5.4 Fiber link simulation results

Pulse propagation through the fiber link is numerically simulated using the generalized nonlinear Schrödinger equation [4], using the experimentally measured input pulse and the fiber parameters shown in table 5.1. We have used the software library SSPROP [33] for the pulse propagation simulations. The numerical simulations solves the nonlinear Schrödinger equation (eq. 2.5) in-

	Dispersion, D (ps/nm/km)	Dispersion slope, S ($ps/nm^2/km$)	Relative dispersion slope, RDS	Effective area, A_{eff} (μm^2)	Nonlinear coefficient, γ ($W^{-1}km^{-1}$)
Standard single mode fiber (SMF), ITU G652	16.5	0.058	$3.5 \cdot 10^{-3}$	82	1.29
Dispersion compensating fiber (DCF), EWBDK	-120	-0.44	$3.5 \cdot 10^{-3}$	21	5.02

Table 5.1: Fiber parameters at 1550 nm.

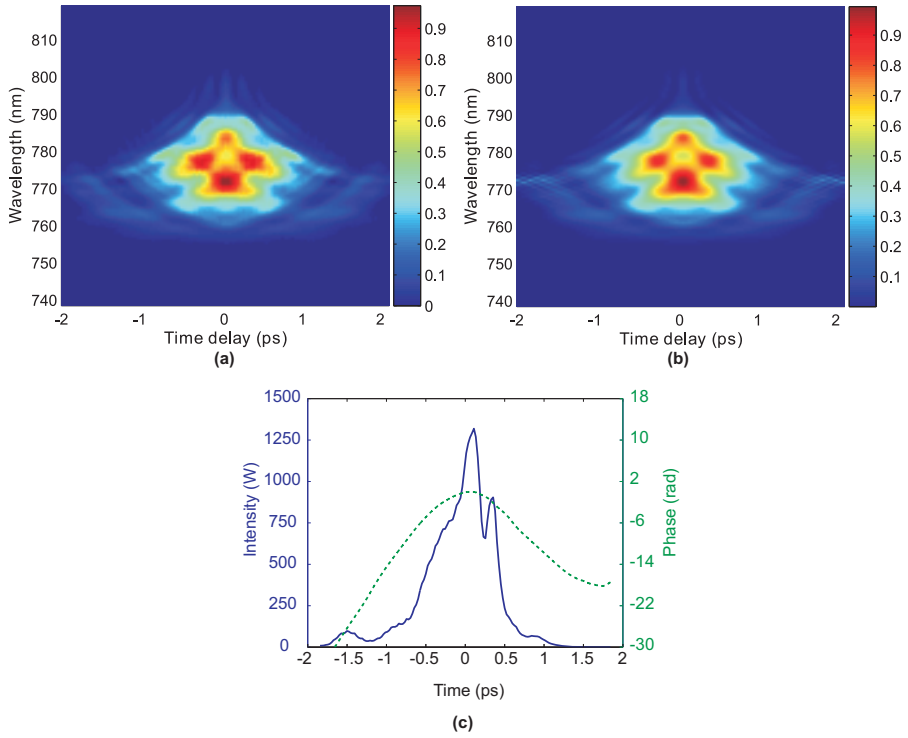

Figure 5.2: FROG characterization of the 1-nJ input pulse. (a) Measured spectrogram and (b) spectrogram of the retrieved pulse. The intensity is normalized to the maximum intensity of each spectrogram. (c) The retrieved pulse intensity (solid, blue curve) and phase (green, dashed curve). The FROG error in the pulse phase retrieval was 1.9% which is acceptable given that all the main features in the measured pulse spectrogram can be found in the retrieved pulse spectrogram. The retrieved pulse is used as input pulse in the pulse propagation software.

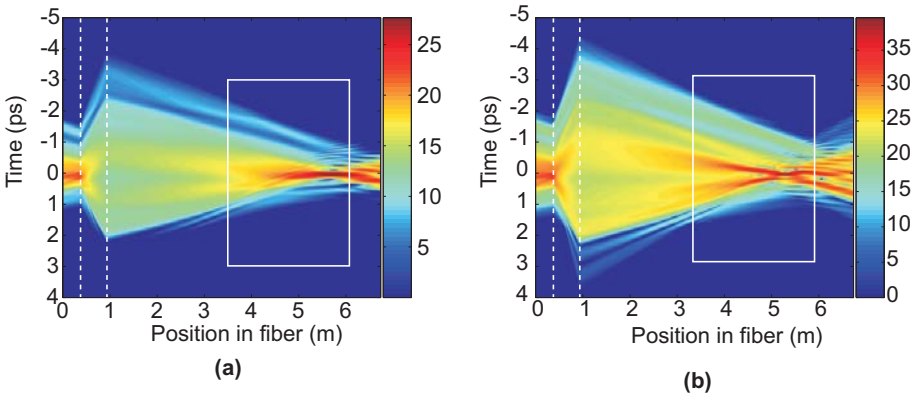

Figure 5.3: Numerical simulation of the pulse propagating through the fiber link with 0.1-nJ input pulse (a) and a 1.0-nJ input pulse (b). The pulse intensity is shown as a function of time and position in fiber link. The intensity scale is in dBW. The white dashed lines indicate the different fiber sections and the white boxes indicate the area where the experimental data is obtained.

cluding third-order dispersion, that is

$$\frac{\partial u}{\partial z} + \frac{\alpha}{2}u + i\frac{\beta_2}{2}\frac{\partial^2 u}{\partial t^2} - \frac{\beta_3}{6}\frac{\partial^3 u}{\partial t^3} = i\gamma\left(|u|^2 u + i\frac{t_0}{2\pi}\frac{\partial\left(|u|^2 u\right)}{\partial t} - T_R u\frac{\partial\left(|u|^2\right)}{\partial t}\right), \tag{5.1}$$

where u is the slowly varying pulse envelope $u(z,t)$ in the reference frame moving along with the pulse at the group velocity, $t = t_0 - z/v_g$ where t_0 is the physical time, and where it is assumed that the electric field propagates in the positive z-direction.

Figure 5.3 shows the results of a numerical propagation of a pulse with low energy (0.1 nJ), and a pulse with higher energy (1.0 nJ). In the low energy case the compression is mainly due to dispersion, and the pulse is compressed to a FWHM duration of 122 fs at the position 5.67 m in the fiber link. The length of the waist region where the pulse is shortest can be defined as the distance between the positions in the fiber link where the pulse is stretched to $\sqrt{2}\mathrm{FWHM}L_{\min}$ where $\mathrm{FWHM}L_{\min}$ is the FWHM duration at the minimum position. For the 0.1 nJ pulse this waist region is 95 cm long. In the 1 nJ case the pulse is compressed at an earlier position in the fiber link due to a combination of dispersion and self-phase modulation [4]. The pulse is compressed to a FWHM duration of 57 fs at the position 5.26 m. The region of the fiber link where the pulse is short is only 28 cm long and after this the pulse breaks up into several pulses.

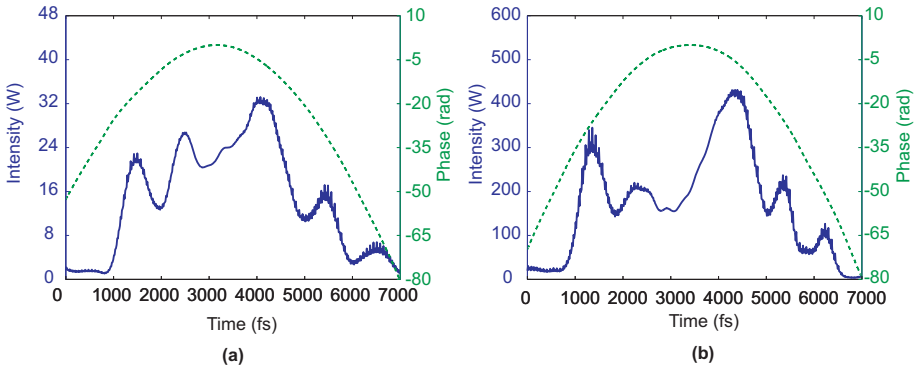

Figure 5.4: Measured pulses after the DCF fiber for a 0.1 nJ pulse (a) and a 1.0 nJ pulse (b).

5.5 Fiber link measurements

The output of the DCF section of the fiber link was measured for different input pulse energies. A small length of SMF was used to couple the light into the measurement setup and the measured pulses correspond to the pulses at position 1.66 m in the fiber link. The energy of the input pulse was adjusted by changing the coupling efficiency in the butt coupling between the fiber laser and the fiber link. The results for 0.1-nJ and 1.0-nJ pulses are shown in figure 5.4. Although minor differences in the pulse shape can be seen when the energy is increased, the overall pulse characteristics after the DCF does not change significantly when the pulse energy is increased from 0.1 to 1.0 nJ, indicating that linear dispersion dominates over SPM in this part of the link, even at 1.0-nJ pulse energy.

The pulse evolution and compression in the SMF fiber was measured in a detailed fiber cutback experiment. Starting at a length of 6.0 m of the fiber link, each cutback removed a few centimeters of fiber and the output pulses were measured for different pulse energies. The fiber piece was cut out from the middle of the SMF fiber and the fiber ends were spliced together again. In this way it was possible to keep the output coupling into the measurement setup fixed. The results for 0.1-nJ and 1.0-nJ pulses are shown in figure 5.5. Since there is no absolute phase information in the SHG-FROG measurements we had to manually align the individual pulses in time with respect to one another. There is a time ambiguity in the SHG-FROG technique and it is not possible a priori to know if a retrieved pulse is oriented correctly on the time axis or if it should be flipped in time. However, here the sign of the chirp of the input pulse is known from the fact that the pulse is compressed in the anomalous dispersive fiber. The retrieved pulse is oriented on the time axis

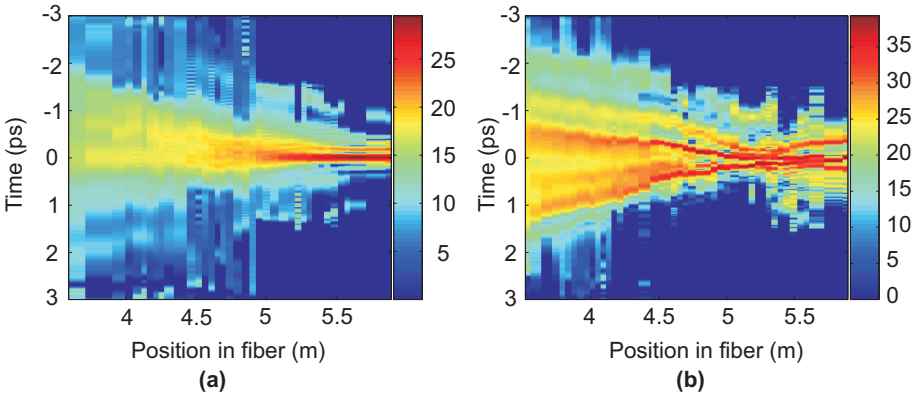

Figure 5.5: Experimental measurements of 0.1 nJ (a) and 1.0 nJ (b) pulses showing the final stage of the compression in the SMF fiber. The pulse intensity is shown as a function of time (vertical axis) and position (horizontal axis) in fiber link. The intensity scale is in dBW. The disintegration of the pulse which was discussed in chapter 2 is clearly seen in the 1.0 nJ case.

such that the chirp has the same sign. The pulses that follow in the fiber link are oriented in time in the same way and aligned with respect to the input pulse.

We see a very good qualitative agreement between the evolution of the pulse shape seen in the experiment (figure 5.5) and in the simulation (figure 5.3). In the low-power case the shortest possible pulse is compressed with a pulse shape which approaches a single peak. The slower compression of the wings of the pulse is visible both in the simulation and the experiment, and there is little pulse break-up after the point of shortest pulse duration. In the high power link, the pulse with the shortest duration consists of several peaks, and we observe a significant reduction of the length of the region where the pulse is short, as well as a strong break-up of the pulse after the point of shortest duration.

Figure 5.6 shows the pulses at the optimum position in the fiber link where the pulses are shortest and where most of the pulse energy is in the center peak. The 0.1-nJ pulse is compressed to a FWHM duration of 84 fs and a peak power of 0.9 kW at 5.62 m which is close to the expected position. The 1.0-nJ pulse is compressed to its shortest duration at 5.27 m, with a FWHM duration of less than 60 fs but with significant energy in the side pulses. The peak power is 6.9 kW.

For this fiber link the main power-handling limitation is the effect that the pulse breaks up into several pulses when the pulse energy is increased. For pulse energies higher than 1.0 nJ we have seen, both numerically and

experimentally, significant pulse breakup and it was not possible to compress and obtain sufficient energy in the main pulse.

5.6 Fiber link for multi-element terahertz imaging

The close similarity between the pulses after the DCF section of the fiber, shown in figure 5.4, indicates that the input pulse energy might be increased even further. A further increase of the input pulse energy will enable an extension to the simple 1x1 link demonstrated in the previous section. By introducing a 1x32 fiber splitter (Ignis Photonyx PLC 1x32) into the fiber link and increasing the pulse energy to 2.6 nJ we are able to provide 32 channels of 100 fs pulses, each with a pulse energy of 0.06 nJ (corresponding to 5 mW average power), sufficient to drive 32 photoconductive THz emitters or detectors. Figure 5.7 shows the fiber link design.

Figure 5.8(a) depicts the simulated pulse intensity along the fiber link, again using the measured output pulse from the laser as input to the simulation. The pulse is compressed in Section I which is SMF and stretched in the DCF part of Section II. The abrupt change in intensity after Section III is due to the 1x32 fiber splitter. Again using the measured input pulse, the simulations show that the pulse can be compressed to a FWHM duration of 100 fs after a total length of 5.65 m fiber. The compressed pulse is shown in 5.8(b).

As in the previous section, the simulation results are validated in a fiber cutback experiment. We have recorded autocorrelation traces for various fiber lengths, across the area where the numerical simulations predicted a minimum

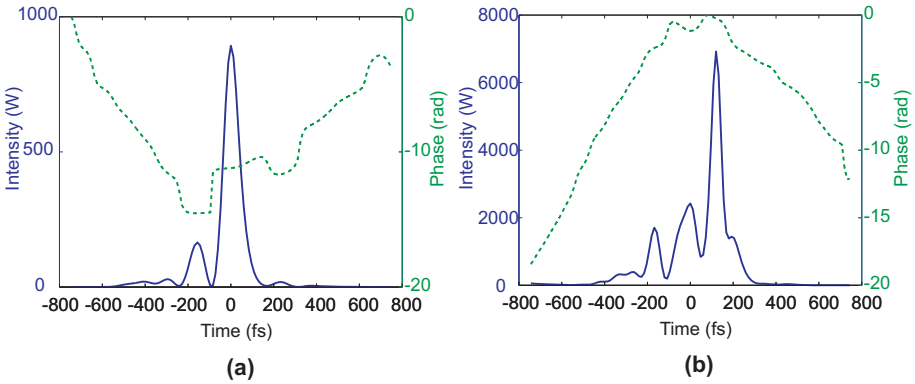

Figure 5.6: The optimum 0.1 nJ (a) and 1 nJ (b) pulses. The pulse envelope (solid line) and phase (dashed line) are shown.

pulse length. Figure 5.9(b) shows a zoomed-in view of the measured autocorrelation functions as function of fiber link. A minimum is seen at about 5.8 m of total fiber link length. At this point the pulse is shortest and the fiber should be terminated and attached to the THz antennas. The development of the autocorrelations along the minimum pulse length shows by comparing the two plots in figure 5.9 for numerical data (a) and measured (b), respectively, very similar features before and after the full compression point. These features are present despite the deviation in the fiber link lengths. The minimum measured autocorrelation FWHM is 99 fs ($\approx$ 80 fs pulse length) at 5.8 m link length. The simulated autocorrelations of the real input pulse from the laser reaches a minimum FWHM of 135 fs at the position of 5.65 m.

Figure 5.10 shows a measured (a) and retrieved (b) FROG trace of the shortest pulse recorded at a position of 5.8 m. The retrieved FROG trace is in good agreement with the measured trace, and exhibits a FROG retrieval error of 1%.

The retrieved pulse intensity and phase are shown in 5.10(c). The extracted pulse intensity exhibit ripples in the trailing edge indicating a complex pulse structure which is expected due to the complex input pulse shape (cf. figure 5.2), and we find excellent agreement with simulation (5.8).

The difference in optimum fiber link length between the measured data and the numerical simulations is 15 cm out of 5.6 m of fiber. We find that this 2.7% deviation is acceptable. The deviation can be explained by uncertainties in the measurement of the fiber link input pulse which showed a FROG-error of approximately 1.9% and uncertainties in the fiber parameters. The optimum fiber link length in the numerical simulations will change much with variations in the dispersion parameters and in the nonlinear coefficients of the used fibers.

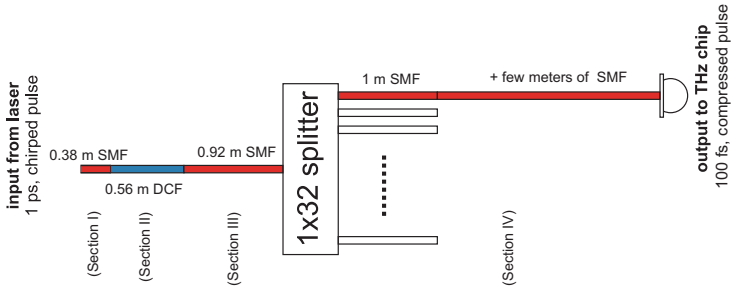

Figure 5.7: Design approach of the multiple-element fiber link between the femtosecond laser and the THz antennas.

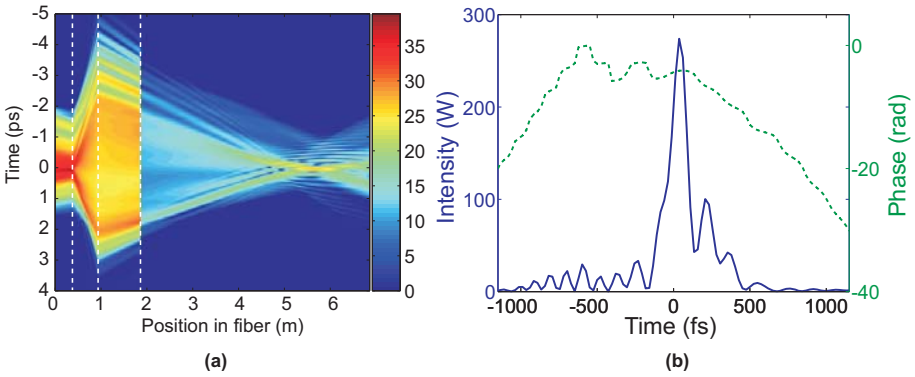

Figure 5.8: (a) 2D plot on a logarithmic scale (dBW) of the simulated pulse intensity as a function of fiber length using the measured output pulse from the laser as input pulse. The dashed line indicates the borderline between the different fiber sections. (b) Plot of the intensity and the phase of the simulated compressed pulse at 5.65 m. The FWHM pulse length is 100 fs.

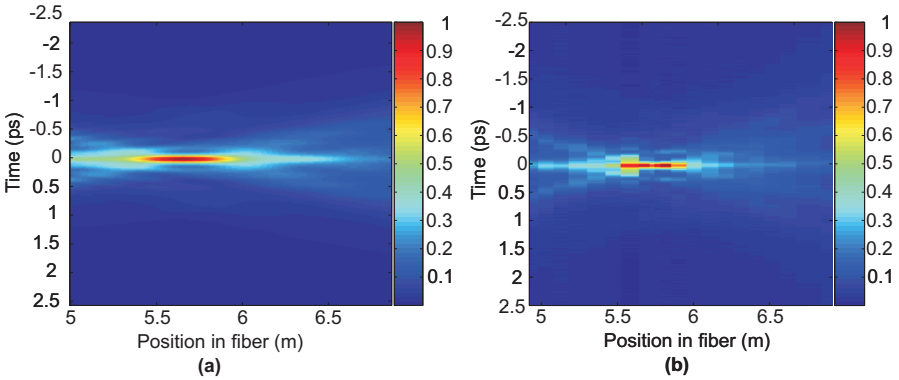

Figure 5.9: (a) Simulated autocorrelation functions of pulses in the fiber link at positions near the point where the pulse gets re-compressed to sub-100 fs pulse length. (b) The measured autocorrelation functions in the cutback experiment. The plots are on a linear intensity scale.

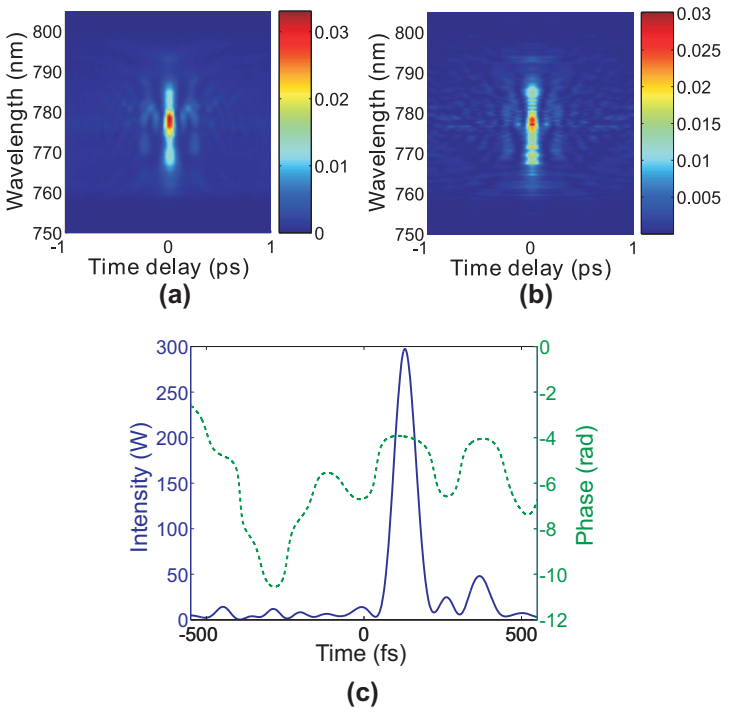

Figure 5.10: FROG characterization of the minimum pulse width. Top row: (a) Measured spectrogram and (b) spectrogram of the retrieved pulse. The intensity is normalized to the maximum intensity of each spectrogram. (c) Plot of the intensity and the phase of the measured retrieved pulse at 5.8 m link length.

5.7 THz pulse generation with the fiber link

We used the output of the fiber link for generation and detection of THz pulses in a standard THz time-domain spectrometer, by excitation of photoconductive dipole antennas fabricated on InGaAs/AlGaAs superlattice structures [63], commercially available from Menlo Systems. Figure 5.11 shows the generated THz pulse in the time domain and in the frequency domain. The THz pulse has a near-single-cycle appearance in the time domain, and a corresponding smooth frequency spectrum spanning the range 0.1-2 THz.

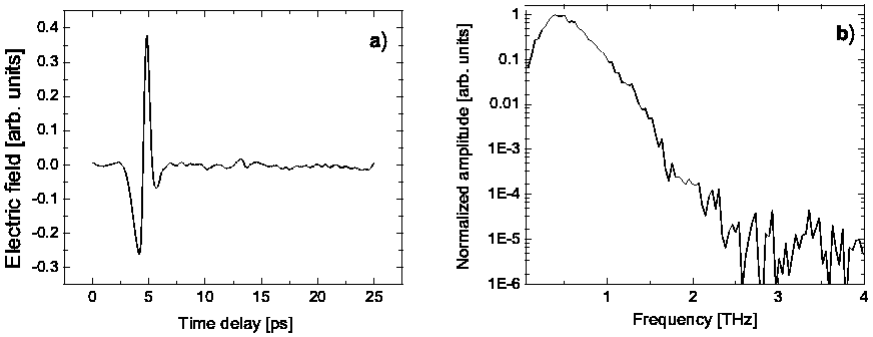

Figure 5.11: (a) THz transient in the time domain and (b) its frequency spectrum generated and detected in photoconductive switches excited by 0.06-nJ pulses from the fiber link.

The spectral amplitude of the generated THz signal has a peak dynamic range of approximately 200, corresponding to 50-dB dynamic range in power. The measurement was done by lock-in detection and chopping of the bias voltage on the emitter at a frequency of 3.2 kHz.

5.8 Further characterization of the single channel fiber link

We will now return to the discussion of the single channel fiber link and comment on some of its limitations. From the discussion in section 2.4 we know that when a linearly chirped pulse is compressed in anomalous dispersive fiber and when the nonlinear length is comparable to the dispersive length then a fraction of the pulse energy, possibly a significant fraction, will end up in the pedestal instead of in the compressed center part of the pulse. This fraction increases with the pulse energy. This is a limitation in this compression scheme which is unavoidable.

Figure 5.12 shows the cutback measurements for a 1.2 nJ pulse in the fiber link with a single transmission channel. The results from numerical simulations are also shown for comparison. With this pulse energy it was not possible to find a pulse which was short enough and at the same time had sufficient energy in the center peak. We therefore found that 1 nJ was an upper link on the pulse energy for this fiber link. The breakup of the pulse that is expected from the numerical simulations can be easily seen in the measurements. The maximum peak intensity which is obtained in the fiber link is slightly higher than in the 1 nJ case. It was not possible to adjust and align the individual pulses on the time axis with respect to one another like in the 0.1 nJ and 1 nJ cases for reasons explained below.

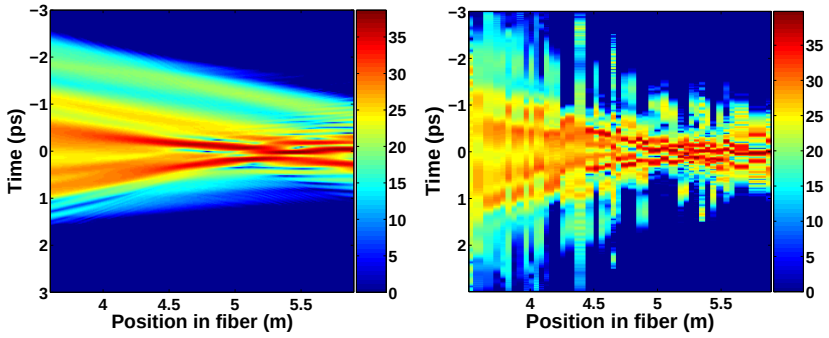

Figure 5.12: Numerical simulations and experimental measurements showing the compression of a 1.2 nJ pulse in the single channel fiber link. The pulse intensity is shown as a function of time (vertical axis) and position (horizontal axis) in fiber link. The intensity scale is in dBW. The retrieved pulses have not been adjusted with respect to one another. The breakup of the pulse discussed in chapter 2 is clearly seen.

Next, we address the question on aligning the individual measured pulses for different cutback lengths with respect to one another in time. In the numerical simulations we assumed a time frame which moved with the group velocity at the center frequency ω_0. For the retrieved pulses it is not a priori clear what the arrival time is. FROG uses a gating of the pulse with itself so there is no absolute time reference in the measurements. Specifically for the FROG that use second-harmonic generation there is also the direction-of-time ambiguity. An interferometer with the fiber link in one arm could tell us the arrival time with respect to a reference pulse and would also solve the time-ambiguity problem. However, the uncertainty in the cutback length will make the uncertainty in position large. E.g. an uncertainty of 0.1 mm in a cutback would give an uncertainty of 0.5 ps in the arrival time. Because of nonlinearities the frequency content of a given part of a pulse will change from one position in the fiber to

the next. In principle, if there is some recognizable feature in the frog traces, e.g. a trailing pulse, then this could be used to align the pulses. It would have to be a low power pulse well seperated from the main pulse such that it was not as susceptible to nonlinearities. As mentioned, the different pulses in the cutback measurements were aligned with respect on one another by inspection. That is, we aligned them by manually placing them one by one on the time axis such that there was a clear trend in pulse evolution from one pulse to the next and such that the pulse evolution along the fiber mimics the behaviour expected from the numerical simulations. This alignment was not possible for the measurements with high pulse energies like in the case with a 1.2 nJ pulse. It was also very difficult for pulses with high pulse energies to tell the pulse direction in time from the phase evolution because of the complex phase changes across the pulses. A straight forward way to improve the measurement results is to do cutback measurements with a smaller step size and use e.g. 1 cm steps in the region where the pulse is compressed.

It is important to have a precise measurement of the input pulse that is used in the numerical simulations. As a consistancy check we compared the measured autocorrelation and the autocorrelation of the phase retrieved pulse and they were in good agreement (figure 5.13). If only the autocorrelation was available then it would have been necessary to make a simple estimate of the pulse duration assuming for example a sech^2 pulse shape. A Gaussian pulse shape would underestimate the peak power which is an important parameter in the compression process. The FROG measurements give us more details on the pulse shape and this is necessary for precise numerical estimates. We repeated the FROG measurement of the input pulse and the phase retrieval several times with similar results. Here we have seen how the FROG measurements can reveal details in the propagating pulse, e.g. a weak peak in the leading part of the pulse, which we can then trace back to the input pulse.

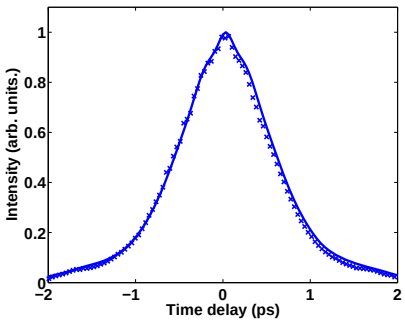

Figure 5.13: Comparison of the measured autocorrelation of the input pulse (blue crosses) and the synthetic autocorrelation of the retrieved pulse (blue line).

Finally, we comment on the quality of the compressed pulses in this compression scheme. Figure 5.14 shows the intensity FWHM of the pulse for different positions in the fiber link and for different pulse energies. Also shown is the fraction of energy in the center peak. The function *fwhm.m* from the SSPROP software package was used to compute the FWHM pulse duration. The function is made in such a way that it only gives an estimate of the FWHM of the main peak in the signal. The energy in the center peak was estimated from the peak power and the FWHM pulse duration by $E_{\text{peak}} = P_0 T_{\text{FWHM}}$. The energy was normalized to the input pulse energy to get the fraction of energy in the center peak. This makes it possible to compare the compression efficiency at different pulse energies. We see that a large fraction, around 75%, of the pulse energy resides in the center peak in the case with low pulse energy, 0.1 nJ, while only 30-40% resides in the center peak in the 1 nJ case. This shows the weakness in this form for compression scheme as discussed above. Pulses with higher pulse energies can be compressed such that the main peak is shorter but it will contain less energy. This is also illustrated if one compares the two pulses in figure 5.6.

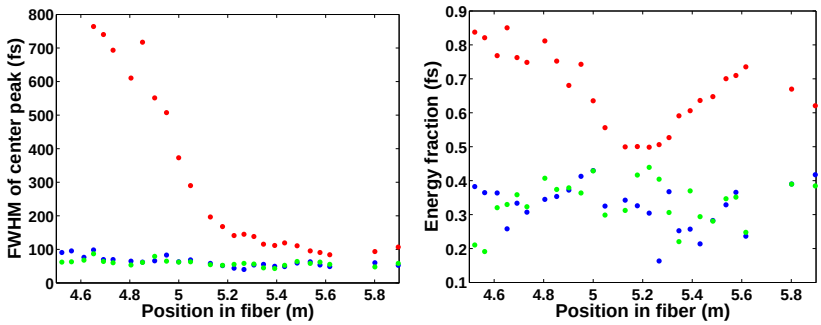

Figure 5.14: FWHM pulse duration (left) and fraction of pulse energy in the center peak (right) as a function of position in the fiber link. Data is shown for three different pulse energies, 0.1 nJ (red dots, upper series), 1.0 nJ (green dots) and 1.2 nJ (blue dots). The positions of the optimum compressed pulses are 5.62 m and 5.27 m for the 0.1 nJ and 1.0 nJ pulses, cf. figure 5.5. The function for computing the FWHM pulse duration clearly underestimates the pulse duration in the region between 4.5 and 5.2 m in the fiber link in both the 1.0 nJ and 1.2 nJ cases. This happens because the pulses already at this point has formed one or two shorter peaks on top of the broad pulse, cf. figures 5.3, 5.5, 5.12.

5.9 Compression as a function of input pulse energy

From figures 5.3, 5.5, 5.12 and from the discussion on pulse breakup in chapter 2 it is clear that the position of the optimum compression point depends on the pulse energy. In a separate experiment we compressed the output of the Toptica fiber laser directly in 75 cm of single-mode fiber in order to study how much the compressed pulse would change if the input pulse power was changed. Numerical simulations (figure 5.15) show that with this fiber length it is possible to obtain a short pulse at an input peak power of 2.3 kW. This was well within the power range of the fiber laser. The pulse is short in the region from 2.1 kW to 2.5 kW. Figure 5.16 show a comparison between measured spectrograms

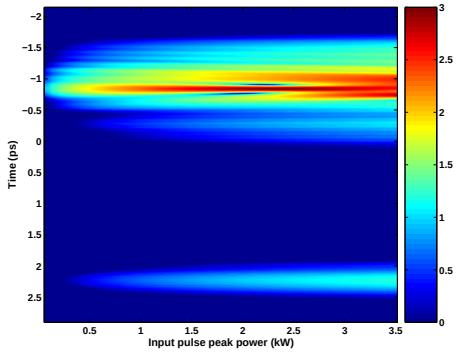

Figure 5.15: Output pulse intensity as a function of time for different input pulse peak powers (dBW intensity scale). There is a weak side pulse following the main pulse. This side pulse was also visible in the input pulse (not shown).

and spectrograms from numerical simulations. The fiber that was used for this experiment had a dispersion parameter D which was a little higher than what was expected at first. This explains the discrepancy between measurements and simulations which is most pronounced in the low power case. Otherwise there is good agreement and we find that the pulse is shortest at approximately 2-2.5 kW as expected.

5.10 FROG errors in cutback measurements

The FROG error increases with measurement number (figure 5.17). There can be several reasons for this. One reason is that the pulses extend over a larger fraction of the time window at earlier positions in the fiber link, i.e. at higher measurement numbers. This can in itself lead to an increase in the FROG error

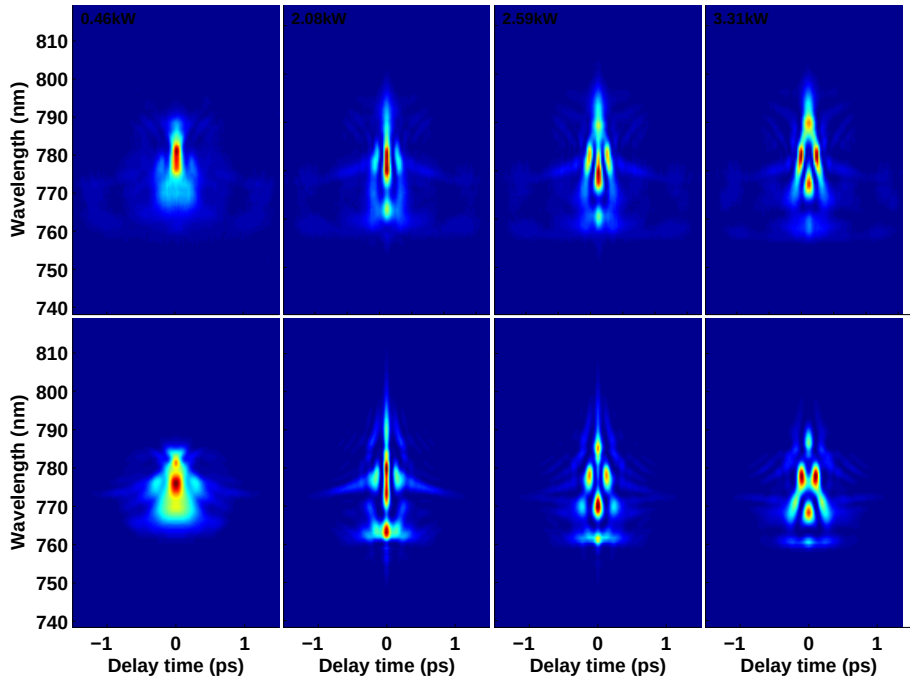

Figure 5.16: Comparison between experimental spectrograms (top row) and spectrograms from numerical simulations (bottom row) for different input pulse peak powers (0.46 kW, 2.08 kW, 2.59 kW and 3.31 kW). Linear intensity scale.

simply because there are more points where the retrieved pulse spectrogram can deviate significantly from the measured spectrogram. This follows from the definition of the FROG error. There have been a few comments on this issue in the litterature [49]. Notice that here we have used two different time windows (figures 5.5, 5.12) - in the region where the pulses are shortest a 3 ps time window was used for phase retrieval and for longer pulses, i.e. at shorter fiber lengths, a 6 ps time window was used. The advantages of using a smaller time window it that the time resolution is larger. There is always a chance that the pulses get clipped if the time window is too small and this is another possible reason for larger FROG errors when the pulses extend more of the time window. Finally, the increasing FROG errors could be explained by the fact that the measurements took place over several days and the alignment of the measurement setup could have changed slightly. Another thing that we can see in figure 5.17 is that retrieval errors for the 1.2 nJ pulse is overall higher than the errors for the 0.1 nJ pulse and this can be explained by the more complex pulse shape in the former case.

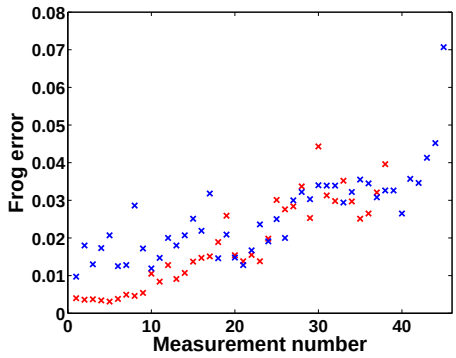

Figure 5.17: FROG error as a function of measurement number for 0.1 nJ (red crosses) and 1.2 nJ (blue crosses) pulses. Incresing measurement number corresponds to earlier positions in the fiber.

5.11 Conclusion

We have demonstrated a fiber link consisting of dispersion-compensating fiber and standard single-mode fiber which can transmit sub-100-fs pulses with energy up to 1 nJ. Our simulations and experimental characterization of the evolution of the pulse shape during the propagation in the fiber link are in good agreement, and we observe the onset of nonlinear effects due to self-phase modulation, resulting in pulse break-up and significant reduction of the optimum

length of the fiber link.

Using high input pulse energies of several nJ we demonstrated that the fiber link is useful for distribution of femtosecond pulses to as much as 32 parallel outputs, with application for instance in advanced multi-element THz systems.

CHAPTER 6

Pulse compression in hollow-core photonic-bandgap fiber with applications in supercontinuum generation

In this chapter we give an experimental characterization of dispersive pulse compression in hollow-core photonic bandgap fibers using frequency-resolved optical gating (FROG). We present results showing the compression of 1028 nm 109 nJ femtosecond laser pulses from a pulsepicked SESAM modelocked ytterbium fiber laser. The pulses are compressed in the part of the transmission window of the hollow-core fiber where the relative dispersion slope is very high, more than an order of magnitude higher than the relative dispersion slope of standard single-mode fiber, and we see interference between different parts of the pulse. As an application we examine supercontinuum generation in nonlinear photonic crystal fibers using the compressed pulses with supercontinuum spectra extending over 900 nm at the -20 dB point. Given that very high peak powers can be transmitted in hollow-core fibers this has potential applications in high-power all-fiber supercontinuum sources.

In section 6.1 we present the experimental setup og discuss the properties of the hollow-core fiber that is being used for the experiment. In section 6.2 we present and compare measurements of the fiber laser pulse before and after propagation in hollow-core fiber with different pulse energies. In section 6.3 pulse propagation in the hollow-core fiber is characterized in a fiber cutback experiments and in section 6.4 we show results on supercontinuum generation with the pulses compressed in hollow-core fiber. This is followed by a discussion of the measurements results in section 6.5.

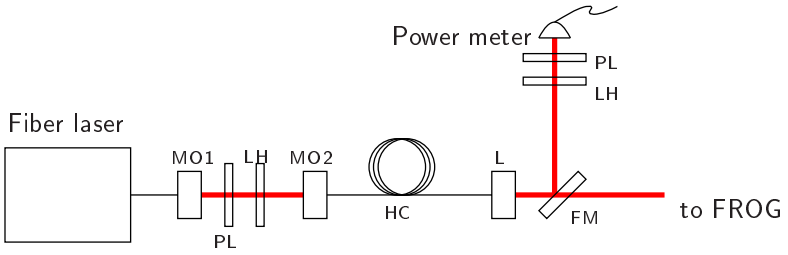

Figure 6.1: Experimental setup. MO1: Microscope objective x10, MO2: Microscope objective x20, L: Aspheric lense f=8.0 mm (Thorlabs, C240TME-B), PL: Polarizer, LH: Half-wave plate, FM: Mirror on flip-mount, HC: Hollow-core fiber.

6.1 Experiment

The experimental setup is shown in figure 6.1. In the experiments we used a SESAM modelocked ytterbium fiber laser [55] (see chapter 4). The fiber laser delivered 0.04 nJ picosecond pulses at 1028 nm with a 31 MHz repetition rate. The output was initially amplified in a polarization-maintaining (PM) ytterbium fiber amplifier and the repetition rate was then reduced by pulse picking to 488 kHz. The output was further amplified in two PM single-mode fiber amplifiers such that the pulse energy was increased to the 100 nJ level.

The output of the fiber laser was coupled into free space using a x10 microscope objective and a polarizer was inserted to make sure that the light was linearly polarized. The light was then coupled into a few meters of hollow-core photonic bandgap fiber (HC-1060-02, NKT Photonics A/S) (see figure 6.3) using a x20 microscope objective. The coupling efficiency was approximately 50%. We then did a series of fiber cutback measurements in which a piece of the hollow core fiber was removed from the beginning of the fiber. With each cutback pulse spectrograms were measured by second-harmonic generation frequency-resolved optical gating (SHG-FROG) using a 40μm thick BBO crystal cut for second harmonic generation of 1028 nm light. In a separate cutback experiment we coupled the output of the hollow-core fiber into a nonlinear photonic crystal fiber and measured the spectra for different fiber lengths.

In general, high quality cleaves of the fiber ends were necessary for an efficient coupling into and out of the photonic crystal fibers. We used a diamond scribe and cleaved the fiber while it was sitting in a bare fiber adapter. In this way we avoided crusching the fragile glass structure. At the beginning of the experiment the hollow core fiber had to be cleaved anew in both fiber ends. In general the coupling efficiency into the hollow fiber dropped over hours. This

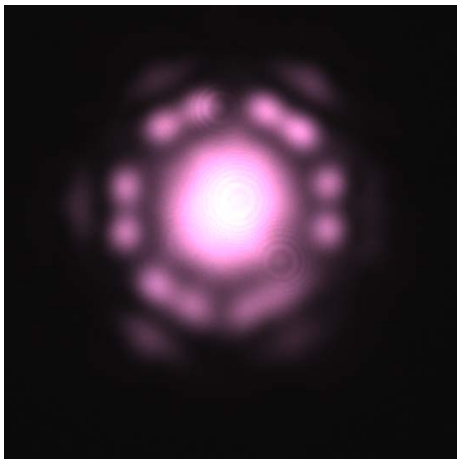

Figure 6.2: The fundamental guided mode of the HC-1060-2 fiber. Most of the light propagates in the core of the fiber with an intensity distribution across the fiber that is close to Gaussian. The light that is visible in the surrounding glass cladding is part of the fundamental mode. The photo was taken by focusing the light from the fiber with a lense (f=6.24 mm, NA=0.4) at a camera CCD chip.

was caused by fiber degradation (see figure 6.3). The degradation was the same at both ends of the fiber and happened over hours which excludes ablation by the coupling light as a possible cause of the problem. Apparently the problem was common for this type of fibers because of the way that it was produced and the degradation does not occur so frequently with newer fibers, according to the manufacturer.

The end piece of the hollow core fiber was left untouched during the cutback experiments. In this way the coupling out of the hollow core fiber and into the FROG setup, or into the nonlinear fiber, stayed intact. Since the coupling efficiency can drop over hours, we continuously made sure that the coupling was intact and recleaved the fibers just before a new experiment if necessary. Typically when doing cutback measurements for fiber loss measurements the input end of the fiber is fixed while the cutbacks are taken from the output end of the fiber. This is done to make sure that the input coupling remains the same which fascilitates precise loss measurements while it is convenient from an experimental point of view because input coupling is only done once. Here we wish to keep the alignment into the FROG measurement setup fixed to minimize any possible changes in the alignment from one cutback to the next.

We found, by coupling into the hollow-core fiber several times while monitoring the optical mode with a CCD camera (see figure 6.2), that if approxi-

mately 50% of the light from the fiber laser was coupled into the fiber then we could be sure that we had coupled into the same mode, i.e. the fundamental guided mode of the fiber.

For each cutback we adjusted the polarization of the input light with a half-wave plate such that the input polarization was parallel to the main axis of the fiber by measuring the optimum polarization extinction ratio (PER) at the output. We used a second half-wave plate and a polarizer at the output end to measure the PER. This was done to avoid that light propagated in two different polarization modes of the fiber since hollow-core fibers in general have a tendency to be birefringent [26]. The fiber was coiled up in a box to minimize polarization fluctuations and the end part of the fiber was fixed to the optical table for the same reasons and for keeping the coupling into the FROG setup intact.

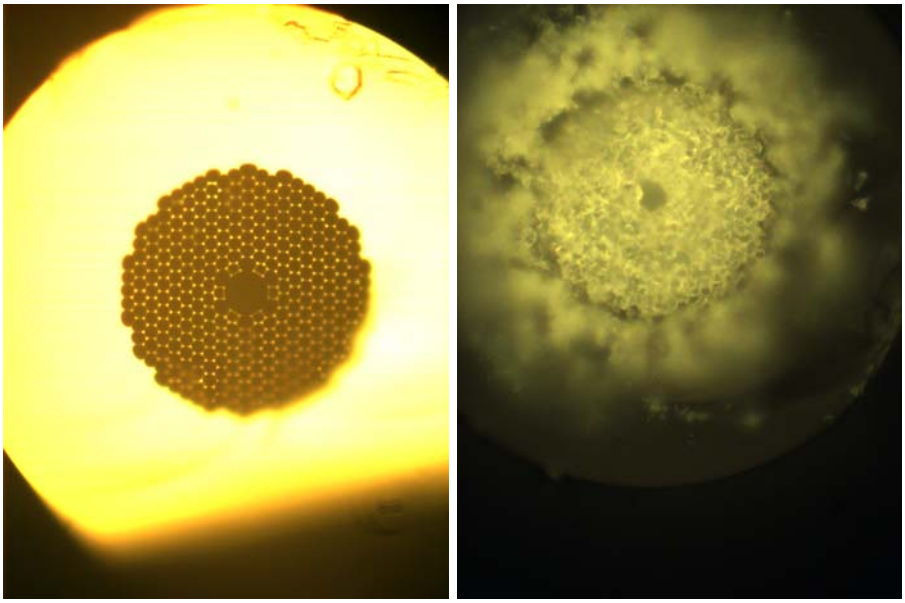

Figure 6.3: The cleaved end facets of the HC-1060-2 fiber when the fiber has just been cleaved (left) and after a few hours where degradation is clearly seen (right). The core diameter is 9.7μm and the length scale is the same in the two pictures. The photonic bandgap structure is clearly seen in the case of a freshly cleaved fiber.

The dispersion and the fiber loss across the fundamental bandgap of the hollow-core fiber, HC-1060-02, is shown in figures 6.4 and 6.5 respectively. The curves showing the dispersion parameter D and the fiber loss are reproduced

from experimental data specified by the manufacturer while the curve showing the dispersion parameter β_2 is derived from D. In general, photonic bandgap fibers can have one or more photonic bandgaps across the optical spectrum. Here we consider only the properties of the fundamental bandgap where the light is best confined and therefore best guided. The core diameter of the fiber is 9.7μm and the mode field diameter is 6.5μm. A photograph showing the light in the fundamental guided mode of the fiber is shown in figure 6.2. More than 90% of the light propagates in air and the effective mode index is approximately 0.99. Both of these values are determined from numerical models and are specified by the manufacturer. The expansion coefficients in a Taylor expansion of the frequency dependent propagation constant $\beta(\omega)$ around 1030 nm are also shown. These are relevant for numerical simulations of pulse propagation in the fiber. Notice that the fiber laser has a center wavelength at approximately 1028 nm where the relative dispersion slope is very high and more than an order of magnitude higher than the relative dispersion slope of standard single-mode fiber at this wavelength.

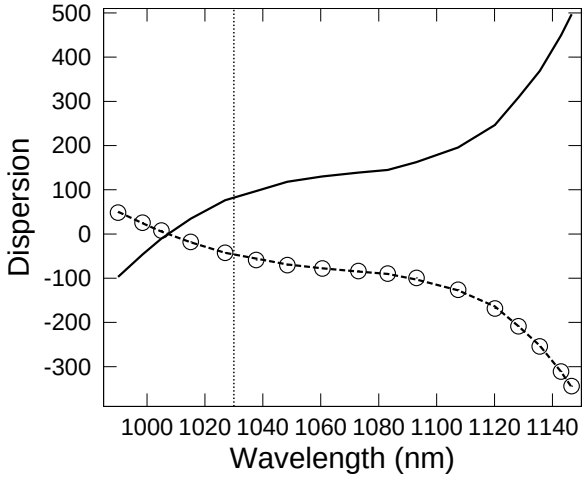

Figure 6.4: Dispersion parameters D (solid line) in ps/nm/km and β_2 (dashed line) in ps^2/km as a function of wavelength. Also shown is a fit (circles) to the β_2 curve with parameters $\beta_2 = -47.8$ ps^2/km, $\beta_3 = 0.93$ ps^3/km, $\beta_4 = 0.015$ ps^4/km, $\beta_5 = -3.8728 \cdot 10^{-5}$ ps^5/km, $\beta_6 = -8.4394 \cdot 10^{-6}$ ps^6/km. The center wavelength is 1030 nm (vertical dashed line). Reproduced from manufacturer data sheet.

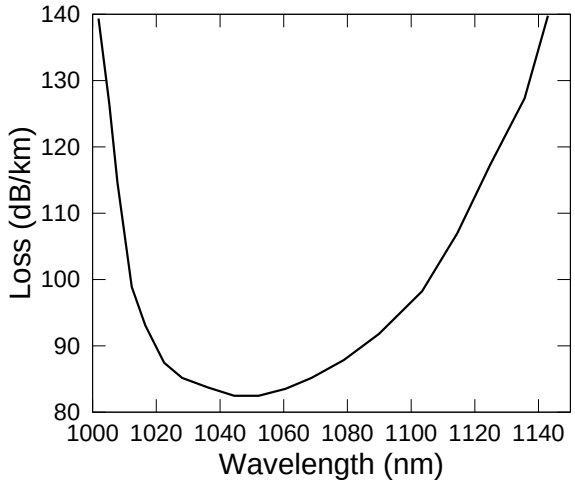

Figure 6.5: Fiber loss as a function of wavelength. The width of the transmission band is larger than 90 nm (defined as the bandwidth over which the loss is < 0.1 dB/km). Reproduced from manufacturer data sheet.

6.2 Dependence on fiber amplifier pump power

In this section we characterize the pulses from the fiber laser for different pump powers in the last fiber amplifier section and compare these with measurements of the same pulses after they have propagated in hollow-core fiber. Figure 6.7 shows measured FROG spectrograms of the pulse at the fiber amplifier output and after propagation in 4.07 m of hollow-core fiber. Spectrograms for three different pump power levels were recorded corresponding to pulses with energies 81 nJ, 109 nJ and 128 nJ (measured after the polarizer and before the hollow-core fiber). Figure 6.6 shows how features in the spectrogram for the 109 nJ pulse can be identified using the independently measured spectrum of the pulse. The alignment of the setup was not changed when we changed the pump power setting. This was important because we want to be able to compare some of the finer changes in the spectrograms when the power changes. A small change in the coupling into the hollow-core fiber will change the pulse shape and/or the polarization of the pulse and a different alignment into the FROG setup can have an effect on the measured FROG spectrogram. There are two main peaks in the pulse at approximately 512 nm (corresponding to 1024 nm in the original pulse) and 518 nm (1036 nm) in the low power output of the fiber amplifier. The two spots at 514 nm come from the sum-frequency signals that

are generated when the pulses at 1024 nm and 1036 nm overlap in time. The time delay between the two peaks is approximately 4 ps. From the individual spectrograms it is not possible to tell a priori which pulse is leading in time because of a time-ambiguity in the SHG-FROG technique. However, when comparing with the spectrograms of the pulses that have propagated in hollow-core fiber and knowing that the pulses propagate in the anomalous dispersive regime of the fiber we know that it is the red part of the pulse that arrives first which is also what we would expect because of a long section of standard panda fiber in the fiber laser system. At high power the blue peak has shifted to approximately 509 nm (1018 nm) because of increased self-phase modulation. At the high pump powers stimulated Raman scattering can be seen in the fiber amplifier output at around 531 nm (1062 nm) in the spectrogram. Only a small part of the Raman scattered light appears in the measured spectrograms but the intensity of the Raman scattered light is also very low (cf. figure 4.10).

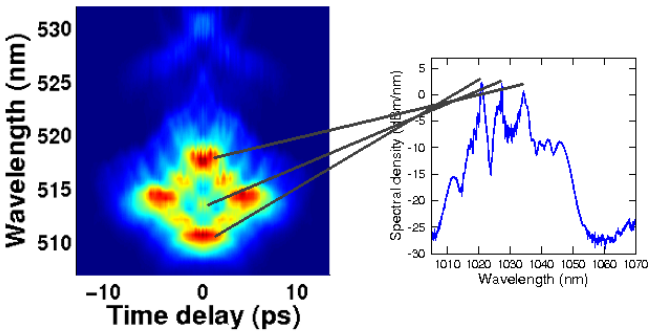

Figure 6.6: Spectrogram and spectrum of the 109 nJ pulse from the fiber amplifier. The peaks in the spectrum can be identified in the spectrogram. Other spots in the spectrogram come from sum-frequency generation of the different peaks at different time delays.

If we move on to an interpretation of the pulses after propagation in hollow-core fiber we can see that the time delay between the two peaks has decreased to 2-3 ps showing that the pulses are getting compressed in time. It appears that the pulse at high pump power is compressed the most, possibly because of its higher pulse bandwidth and we can see that the peak at 1036 nm is compressed more than the peak at 1018 nm which is also expected from the dispersion curve. The Raman scattered light is not visible when the pulse has propagated through hollow-core fiber except for a very weak signal in the high power case (not visible in the spectrogram shown here). From the fiber loss

curve (figure 6.5) we know that the Raman scattered light propagates well within the bandgap and that the fiber loss at this wavelength is comparable to the loss experienced by the main pulse.

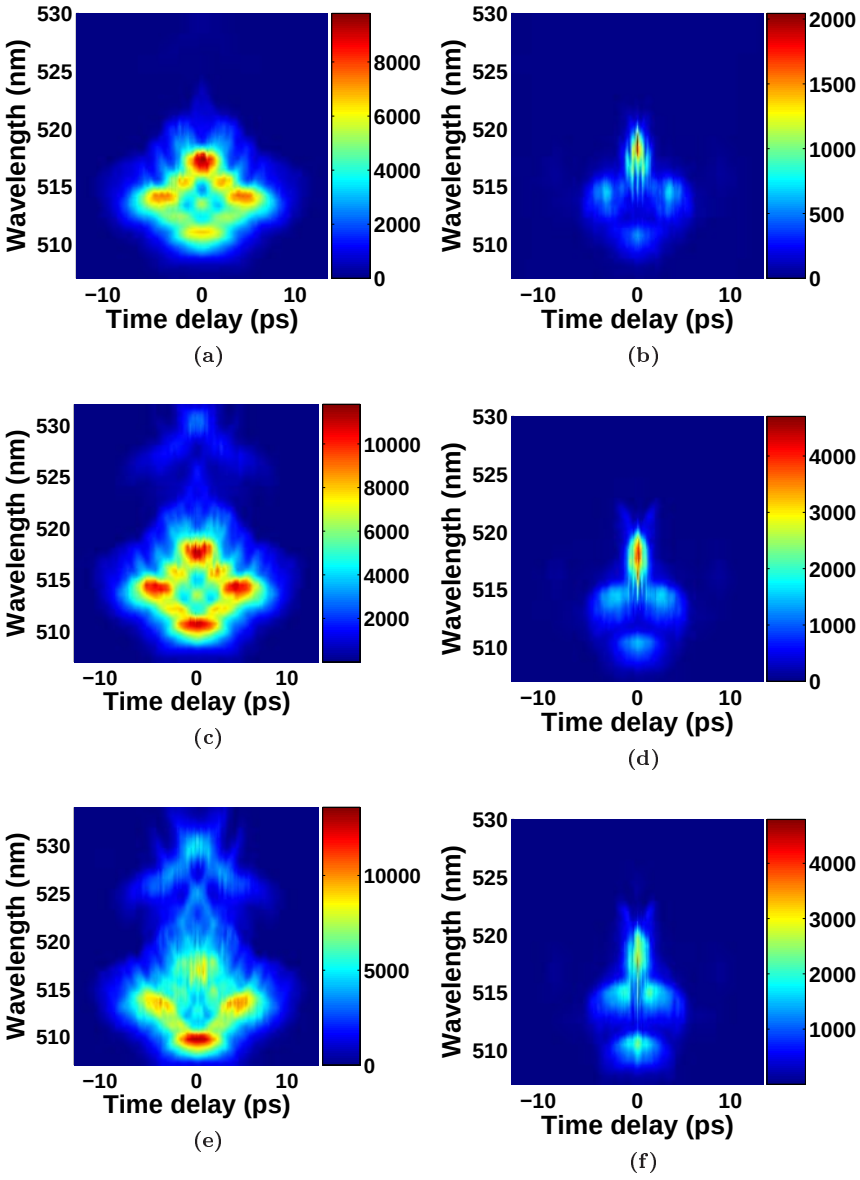

Figure 6.7: FROG spectrograms of the pulse immidiately after the fiber amplifier (left column) and the same pulse after 4.07 m hollow-core fiber (right column) for three different pump powers corresponding to the pulse energies 81 nJ (a),(b), 109 nJ (c),(d) and 128 nJ (e),(f). Notice that the wavelength scale is slightly different in (c) and (e). The colorbar shows the intensity (linear scale) and is normalized to the maximum intensity, i.e. the number of counts in the grating spectrometer, of each spectrogram.

6.3 Fiber cutback measurements

Figure 6.8 shows measured FROG spectrograms for different lengths of hollow-core fiber with the pulse from the fiber amplifier a pulse energy of 109 nJ. Approximately 50% of the light was coupled into the hollow-core fiber such that the pulse energy in the fiber was approximately 55 nJ. The spectrogram of the pulse from the fiber amplifier with this pulse energy was shown in figure 6.7. This pulse energy lies in the middle of power range that was available with our fiber amplifier and the pulse energy was reasonable with only a small fraction of the pulse light lost due to stimulated Raman scattering. At higher pump power levels the pulse energy is increased which in turn leads to increased self-phase modulation and stimulated Raman scattering in the fiber amplifier itself. Autocorrelation traces that correspond to the spectrograms are shown in figure 6.9. They are obtained by integrating the spectrograms over the wavelength. The autocorrelation give an overview of the how the total pulse energy is distributed in time but it is difficult to get much information from these alone. Notice that the time axis in these spectrograms is different from the one used in the previous shown spectrograms. The light around 518 nm (1036 nm) was compressed the most in the range from 4.65 m to 5.52 m to an estimated pulse duration of 200 fs or less. From the input pulse measurements we know that there the main part of the light in the pulses is located at approximately 511 nm (1022 nm) and 518 nm (1036 nm) assuming that fiber nonlinearities are negligible at these pulse energies. In the FROG spectrograms we see a signal at 514-515 nm which is the sum-frequency signal from the two peaks. With increasing fiber lengths more light is seen in the sum-frequency signal at 514-515 nm. This is seen as a lower contrast between the peaks at 514-515 nm and 518 nm because the individual spectrograms are normalized to the maximum recorded intensity in the spectrogram. The increased sum-frequency signal at higher fiber lengths indicate that the peak at 1022 nm is getting shorter compared to the peak at 1036 nm and that the peak at 1036 nm has reached its maximum compression. This is expected because the dispersion is higher by approximately 50% at 1036 nm compared to the dispersion at 1022 nm. Vertical stribes can be seen in the spectrograms in the sum-frequency signal at 514-515 nm at longer fiber lengths and the spacing of the stribes decreases with fiber length such that there are approximately 5 stribes per 2 ps at 4.55 m and 8 stribes per 2 ps at 6.88 m. At 4.55 m the stribes are tilted slightly such that the spacing between them is smaller at shorter wavelengths and oppositely at 6.88 m. We attribute these stribes to interference when different parts of the pulse start to overlap because of the nonlinear chirping of the pulse in the fiber amplifier. The stribes are vertical which indicates that the frequency difference between the different parts of the pulse that cause the interference is almost constant in the overlap region. The red part of the pulse is compressed faster than the blue part and therefore the frequency spacing gets smaller quicker in

the red part of the sum-frequency signal. The spacing of the stribes indicate a frequency difference of approximately 1 THz which is less than the frequency difference of 3.9 THz between the peaks at 1022 nm and 1036 nm.

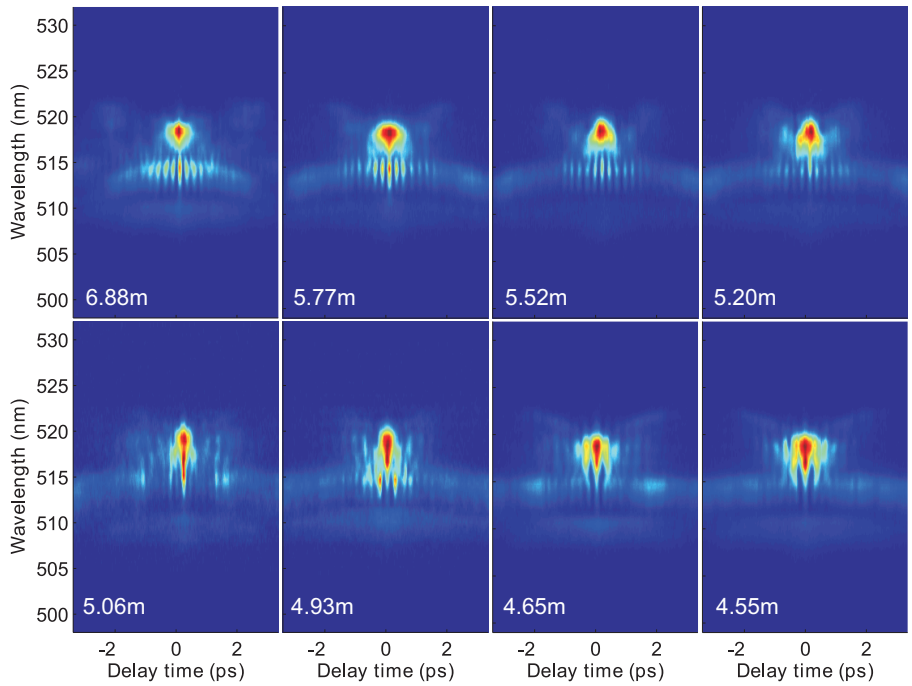

Figure 6.8: FROG spectrograms for different lengths of hollow-core fiber. The intensity is normalized to the maximum intensity of each spectrogram.

6.4 Supercontinuum generation with compressed pulses

Next we investigate supercontinuum generation in nonlinear photonic crystal fiber (PCF) with the pulses compressed in hollow-core fiber. We use a 1 m nonlinear photonic crystal fiber for spectral broadening and supercontinuum generation. The fiber has a 3.5 μm mode field diameter and a zero-dispersion wavelength at approximately 1000 nm. Light was coupled into the nonlinear fiber with an efficiency of approximately 25%. Figure 6.10 shows the measured spectra (measured with an optical spectrum analyzer, OSA, with 5 nm resolution) as a function of hollow-core fiber length. Results for four different input

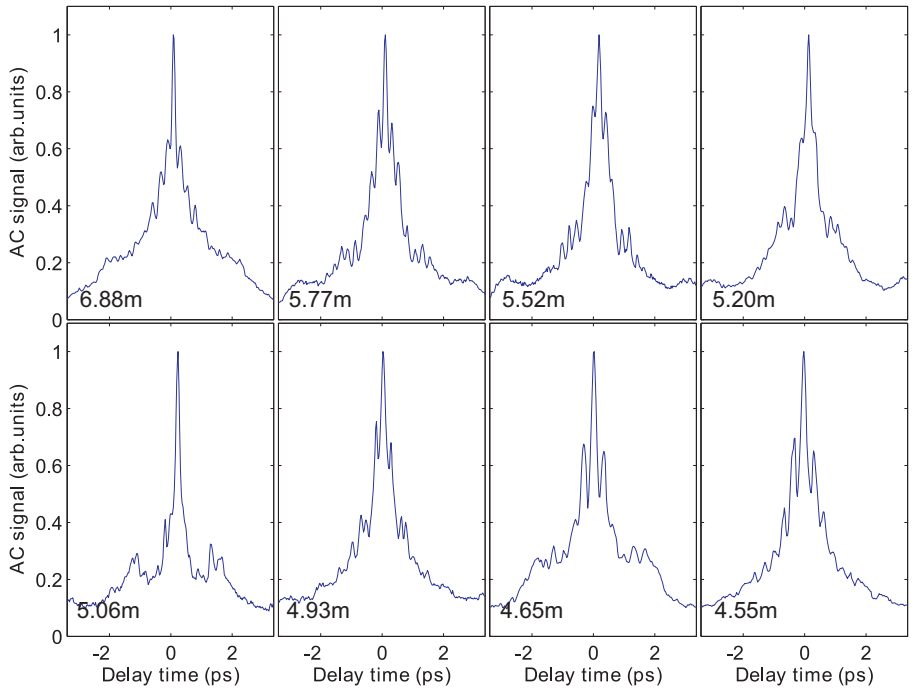

Figure 6.9: Autocorrelation traces for different lengths of hollow-core fiber corresponding to the FROG measurements in figure 6.8.

pulses with pulse energies in the nonlinear fiber of 7.6 nJ, 10.2 nJ, 11.0 nJ and 12.0 nJ (corresponding to pulse energies of 81 nJ, 109 nJ, 118 nJ and 128 nJ before the hollow-core fiber) are shown. The coupling efficiency changed slightly from one cutback to the next such that the pulse energy varied up to 2%. We include the spectrum measured with 0.58 m of hollow-core fiber. This represents the supercontinuum generated with the pulse coming directly from the fiber amplifier, i.e. before pulse compression, but we let it propagate in a short piece of hollow-core fiber to fascilitate a comparison with the compressed pulses on equal terms.

The supercontinuum spectrum goes from 650 nm to 1500 nm with 3.2 m hollow-core fiber and 10.2 nJ pulses. The supercontinuum extends further out into the red and blue part of the spectrum for longer hollow-core fiber lengths which is expected because the pulses are compressed. The spectra at 4.50 m are the broadest and does not seem to follow the same trend as the other spectra. This could be because of a slightly higher input pulse energy. In all cases the

supercontinuum extends further with increasing pulse energy except for 12.0 nJ pulse which, when compared to the 11.0 nJ case, extends more into the red but less into the blue region of the spectrum. We have not found an explanation for this but it could be related to high contribution of Raman scattered light in the 12.0 nJ pulse. The broadest supercontinuum spectrum that was generated extended over 900 nm at the -20 dB point.

Figure 6.11 shows the measured supercontinuum spectra as a function of input pulse energy. Results for different hollow-core fiber lengths are shown. The pulse energy was a little lower in the 4.93 m measurement (7.4 nJ) compared to the 3.8 m measurements (7.6 nJ) which can explain why the supercontinuum spectra are not as broad in the former case. The spectra at longer fiber lengths are more noisy which could be related to the higher peak power and therefore a higher degree of spectral broadening since the pulses are compressed more at these fiber lengths.

6.5 Discussion and conclusion

In these experiments we did not investigate the noise of the generated supercontinuum but it would otherwise be interesting to do so. A possible noise source in this experiments was changes in the coupling efficiency because of beam pointing instabilities. In the setup there are three places where the light is coupled out into free space and back into fiber. This kind of instability can be minimized in an all-fiber solution where the different fibers are spliced together. However, it is not a trivial task to splice photonic crystal fibers together with low loss. Low loss splicing of hollow-core fiber and standard panda fiber has been demonstrated [26]. Another advantage of an all-fiber solution besides from added stability is that it is very compact. The problems with degradation of the end facets of the fibers would possibly also be eliminated in an all-fiber system.

In conclusion, we have presented experimental measurements showing dispersive pulse compression in hollow-core photonic bandgap fiber. Frequency-resolved optical gating was applied and we showed how the long wavelength part of the spectrum of the pulse from a fiber laser system was compressed before the short wavelength part of the spectrum. The pulses were compressed to a pulse duration of less than 200 fs but with a significant fraction of light in the wings of the pulse. The pulse energy of the compressed pulses was approximately 55 nJ. As an application we demonstrated supercontinuum generation in nonlinear photonic crystal fibers with spectra extending over 900 nm at the -20 dB point. This has possible applications in high-power all-fiber supercontinuum sources.

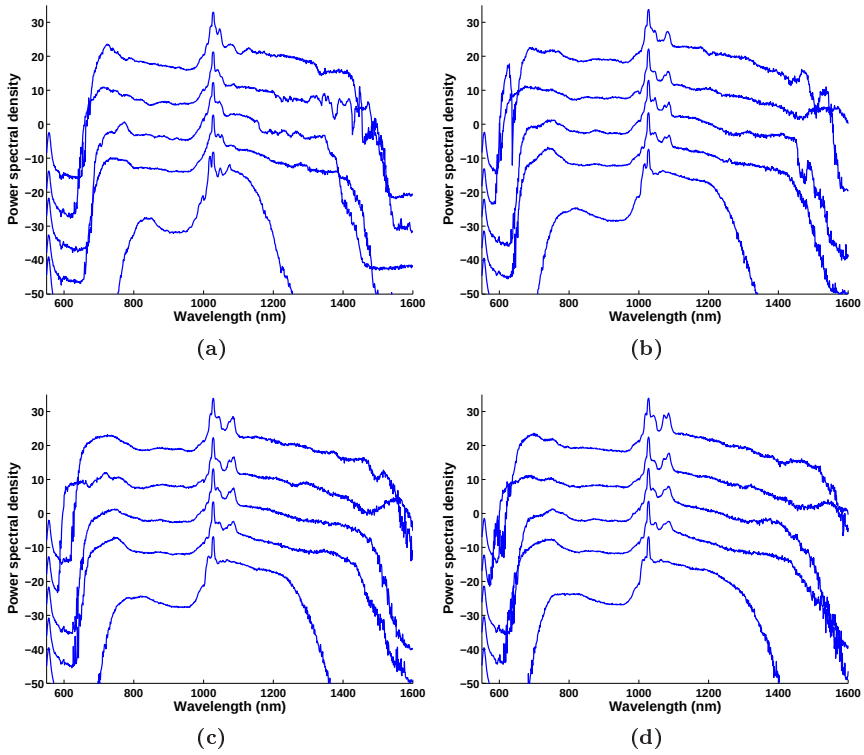

Figure 6.10: Supercontinuum spectra generated in nonlinear photonic crystal fiber as a function of compression, i.e. for different lengths of hollow-core fiber. The fiber lengths are 4.93 m (top curve), 4.50 m, 3.8 m, 3.2 m and 0.58 m (bottom curve). Results are shown for four different input pulse energies 7.6 nJ (a), 10.2 nJ (b), 11.0 nJ (c) and 12.0 nJ (d).

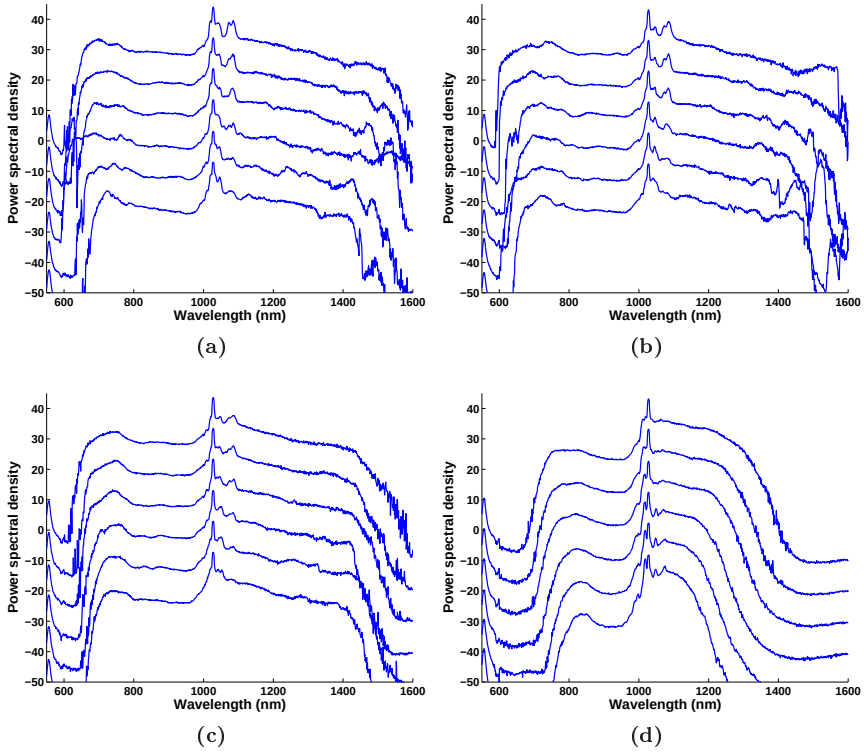

Figure 6.11: Supercontinuum spectra generated in nonlinear photonic crystal fiber as a function of pulse energy. The pulse energies are 7.6 nJ (bottom curve), 8.6 nJ, 9.2 nJ, 10.2 nJ, 11.0 nJ and 12.0 nJ (top curve). Results for 4.93 m (a), 4.37 m (b), 3.17 m (c) and 0.58 m (d) of hollow-core fiber are shown.

CHAPTER 7

Conclusion and outlook

In this thesis I have presented numerical and experimental results for optical fiber links that have been developed for transmission and compression of nanojoule femtosecond laser pulses from fiber laser based systems. We now summarize the main results and conclusions and we comment on some of the things that could be done for improving the performance of optical fiber links.

In the first part of the thesis we gave an introduction to the research field and we presented the numerical expressions needed for numerical simulations of pulse propagation in the fiber links. A significant part of the work done included construction of an experimental setup for pulse characterization using second-harmonic generation frequency-resolved optical gating (SHG-FROG). In the thesis we gave a short introduction to the FROG technique and the experimental setup was described in detail. The setup is now being used extensively in the laboratory for characterization of different lasers and it is currently being used for cross-correlation measurements of pulses from separate fiber links. We have shown how frequency-resolved optical gating give precise measurements of the optical pulses which can then be used for precise numerical simulations of pulse propagation in optical fibers. In general it is of interest to be able to measure an optical pulse which is used as a pump pulse for an experiment and then study the outcome of an experiment using this input pulse. An example of this is the experiments with supercontinuum generation in nonlinear photonic crystal fiber that was presented in this theses. It could also be interesting to do an experiment along these lines where one directly maps a measured femtosecond pulse with a terahertz pulse generated with either photoconduc-

tive switches or optical rectification [65]. It is possible to measure the electric field of terahertz pulses directly by e.g. electro-optic sampling and it could be interesting to study the terahertz generation process.

For the experiments we constructed an all-polarization-maintaining SESAM modelocked picosecond fiber laser with a 1028 nm center wavelength with free-space pulse picking and amplification in polarization-maintaining fiber amplifiers based on Yb-doped active fiber as the gain medium. The first version of laser had a repetition rate of 34 MHz, and maximum output power of 440 mW, which corresponds to a pulse energy of 13 nJ. The pulses could be compressed to femtosecond pulses with pulse durations of approximately 150 fs in a free-space-coupled grating based compressor at the end of the system. The second version of the laser oscillator had a repetition rate of 31 MHz and the output of the oscillator was pulse picked and further amplified which resulted in pulse energies up to 164 nJ at a repetition rate of 489 nJ. Higher pulse energies would be interesting for a number of applications, e.g. high-power supercontinuum generation or research in soliton excitation in hollow-core fiber.

Experimental results for two different types of fiber links were presented in the thesis. The first fiber link consisted of dispersive compensating fiber and compression in standard-single mode fiber. The fiber link was designed for compression of chirped femtosecond pulses from a commercial 1550 nm fiber laser. Pulse energies up to 1 nJ were transmitted. Our simulations and experimental characterization of the evolution of the pulse shape during the propagation in the fiber link were in good agreement, and we observed the onset of nonlinear effects due to self-phase modulation, resulting in pulse break-up and significant reduction of the optimum length of the fiber link. Using higher input pulse energies of several nJ we demonstrated that the fiber link is useful for distribution of femtosecond pulses to as much as 32 parallel outputs, with application for instance in advanced multi-element THz systems.

The second fiber link consisted of hollow-core photonic-bandgap fiber and made it possible to compress pulses with higher pulse energies, up to 55 nJ, from our amplified ytterbium fiber laser at 1028 nm. We presented experimental FROG measurements showing the dispersive pulse compression in the fiber. Pulses were compressed to a pulse duration of less than 200 fs but with a significant fraction of light in the wings of the pulse. As an application we demonstrated supercontinuum generation in nonlinear photonic crystal fibers with spectra extending over 900 nm at the -20 dB point. This has possible applications in high-power all-fiber supercontinuum sources. The supercontinuum generation process is different in the femtosecond and the picosecond regimes and it could be interesting to study the generated supercontinuum and its noise properties as a function of compression in more detail [66]. In could also be interesting to extend the study to pulses with higher pulse energies to study soliton formation in the hollow-core fiber and to study supercontinuum

generation with these solitons. Solitons would be best excited with pulses that were not initially chirped as much as the pulses from our current fiber laser. For high-power chirped pulses we would expect to see pulse breakup similar to what we have seen for low-power nanojoule pulses in standard single-mode fiber. It is difficult to increase the nonlinearity of the hollow-core fiber without increasing the dispersion, in order to lower the pulse energy needed for soliton formation [18].

In both fiber link applications the generation of light at other frequencies, either terahertz radiation or supercontinuum radiation at optical frequencies, is much dependent on the input pulse duration and pulse shape and therefore a careful characterization of the optical pulses was necessary. The compression scheme, that is, the compression of chirped picosecond pulses in anomalous dispersive fiber, was the same in both types of fiber links. However, it was possible to compress pulses with higher pulse energies in hollow-core fiber because the light propagates in the air core of the fiber and the nonlinearity of the fiber is orders of magnitude lower than the nonlinearity of standard silica fibers. We did not see any nonlinear effects, i.e. any spectral changes, in the hollow-core compression measurements. The hollow-core fiber that was used has anomalous dispersion at the wavelengths of ytterbium fiber lasers and was therefore suitable for compression of the pulses from the fiber laser. In general, standard silica fibers are normal dispersive below 1300 nm. Nonlinear photonic crystal fibers and tapered silica fibers are other examples of fibers that can have anomalous dispersion at ytterbium fiber laser wavelengths and at even shorter wavelengths as well but these fibers are, of course, highly nonlinear and therefore not suitable for fiber link applications.

APPENDIX A

Pulse Picker Electronics

The purpose of the pulse picker electronics is to make a suitable nanosecond trigger pulse for a radio-frequency (rf) driver. The rf driver is connected to an acousto-optic modulator (AOM) that can be used to switch individual pulses from an optical pulse train with a MHz repetition rate.

The pulse picker electronics (see figure A.1) is triggered by the signal from a fast optical pulse detector. The electronics counts the number of pulses and after a certain number of pulses it sends out a nanosecond long square pulse that goes into the rf driver. We designed the electronics such that it was suitable for lasers with pulse repetition rates up to 40 MHz. A 40 MHz pulse repetition rate corresponds to a period of 25 ns and this is the time window that is available for the rf trigger pulse. If the rf trigger pulse extends over more than one period then more than one optical pulse is transmitted which is not the intension. It also has to be taken into account that the rf driver has a rise time of a few nanoseconds and that it takes a few nanoseconds before the rf pulse extends over the whole AOM crystal. The rf driver (MODA250-D2-33, A-A Opto-Electronic) has a 250 MHz carrier frequency and 3 ns rise/fall time. The acouto-optic modulator (MT250-A0,2-1064, A-A Opto-Electronic) consists of a 0.2x1 mm^2 TeO2 crystal and electrodes. The rise time depends on the beam diameter and is 13 ns for a 80 μm focused beam. In conclusion, the characteristic times for the electronic components, e.g. rise and fall time for the integrated circuits, have to be on the order of a few ns or less. Here we used TTL buffers for adjusting the trigger pulse delay with respect to the optical pulse train and for setting the pulse length. Another more elaborate

solution would be to use a programmable FPGA integrated circuit.

We tested the electronics with a fiber oscillator with a repetition rate of 31 MHz. There was 3 mW of optical power in the monitor signal which was detected on a Thorlabs PDA10A and monitored on an oscilloscope with a 50Ω input impedance. The input signal was 6 ns long and had a maximum amplitude of 275 mV and a 0 V ground level. When measured with a 1 MΩ input impedance the maximum amplitude was approximately 450 mV and there was a 50 mV ground level. A summary of the specifications of the electronics is shown below.

Input pulse repetition rate	up to 40 MHz
Requirement for optical detector signal ampl.	$>$ 50 mV
Rf trigger pulse duration	10-40 ns (3 ns steps)
Rf trigger pulse delay	0-30 ns (3 ns steps)
Output voltage amplitude (with 50 Ω load)	0.6-2 V

A.1 Circuit diagrams

Input stage with comparator

The input stage circuit is shown in figure A.2. The comparator (ADCMP600) has a 4 ns rise time at 5.5 V (where the rise time is defined as the time it takes the comparator to go from 10% to 90% of the output voltage). The comparator is not designed to handle a capacitive load, like e.g. a transmission line, and therefore a TTL buffer is inserted immediately after the comparator. Several 10nF capacitors close to the +5 V supply input to the comparator are necessary for stability and for the same reason the use of a ground plane is recommended. A 50Ω resistor is used at the input for impedance matching since the circuit is inserted after a transmission line, i.e a coaxial cable from the pulse detector. The threshold voltage is between 0 and 1 V and is set by the voltage divider with R1=50Ω and R2=3.5kΩ.

Counter circuit

The counter circuit (not shown) consists of a 74F269 and a switch.

Circuit for making a nanosecond pulse with variable length and delay

It is necessary to be able to set the length of the trigger pulse and the delay of the trigger pulse with respect to the optical pulse train in order to make sure that there is maximum rf modulation at the time when the optical pulse passes through the crystal. The delay is determined by the delay in the electronics and in the coaxial cables connecting the pulse detector, the electronics and the

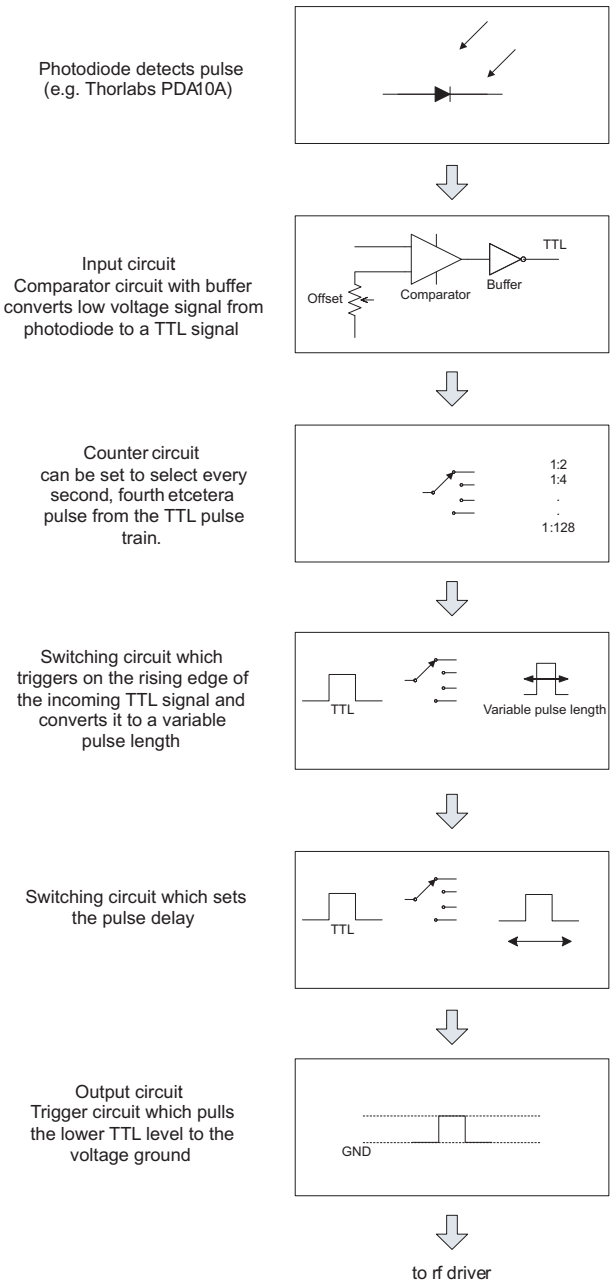

Figure A.1: Overview of the pulse picker electronics.

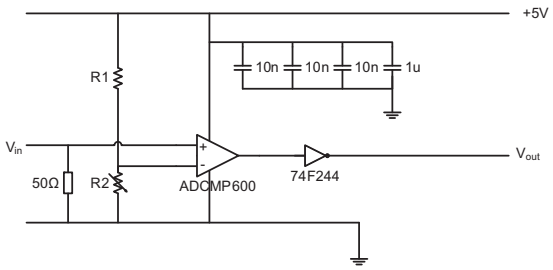

Figure A.2: Input stage with comparator.

AOM crystal. In figure A.3 is shown the circuit that is used to set the pulse length. The TTL signal from the counter is divided into two pulses. The first pulse goes directly to the flip-flop (74F74) and sets it to high voltage, i.e. this is the onset of the output pulse. The flip-flop stays high until the other pulse which has been delayed in the TTL buffers arrives. The delay in a single TTL buffer is 2-3 ns. The delay circuit design (not shown) is similar to the pulse length circuit but without the flip-flop.

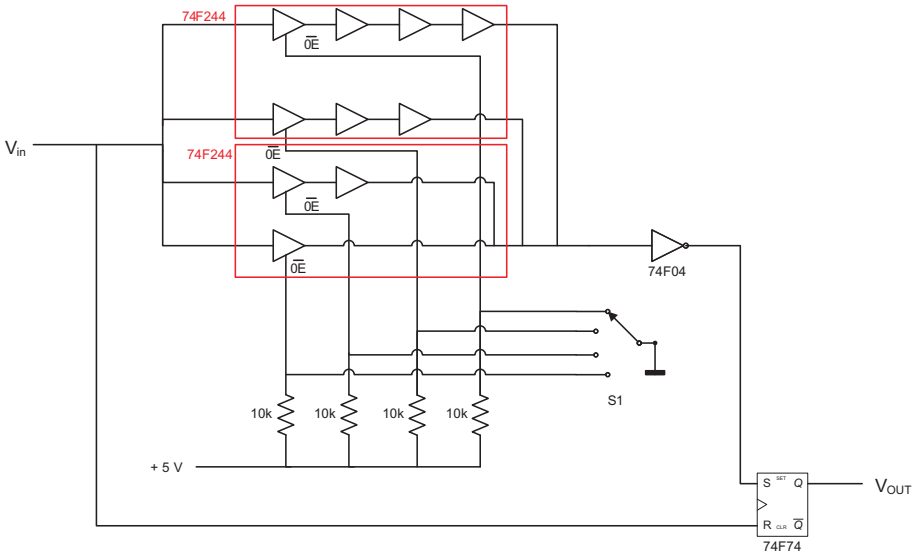

Figure A.3: Circuit for setting the pulse length.

Output stage: From a TTL pulse to a pulse with 0 V offset

The output component is an ADG719 CMOS switch. It is used for high-speed switching and has a -3 dB bandwidth of 200 MHz. This makes it faster than the TTL components used. It also maintains 0 V at the output when the switch is off. This is contrary to the TTL low voltage which can be a few hundred mV. It is necessary to have a 0 V ground level to avoid rf modulation when there is no trigger pulse.

APPENDIX B

The pulse amplitude and the energy density spectrum

Normalization of the pulse amplitude

The pulse amplitude $A(z,t)$ is normalized such that

$$|A(z,t)|^2 = P(z,t),$$

where $P(z,t)$ is the optical power. The Fourier transform of $A(z,t)$ is the amplitude spectrum $\tilde{A}(z,\omega)$ measured in the SI unit $\sqrt{W}$·s. The spectrum, or more precisely the energy density spectrum, is $|\tilde{A}(z,\omega)|^2$ which has the unit W·s^2 = W·s/Hz. In other words the spectrum is the energy per frequency interval. It differs from the power spectral density which is the power per frequency interval. The power spectral density is measured with the optical spectrum analyzer (OSA) and we usually just call it the spectral density. Parseval's relation says that

$$\int_{-\infty}^{\infty} |A(z,t)|^2 dt = \frac{1}{2\pi} \int_{-\infty}^{\infty} |\tilde{A}(w,t)|^2 d\omega$$

That is, the integral over the optical power and the integral over the spectrum both gives the energy of the pulse.

Normalization of FFT spectra in e.g. MATLAB

There is no normalization in the Fast Fourier Transform function fft in MATLAB so the size of $\tilde{A}(\omega)$ will just increase with the number of fft points N. In

the inverse Fast Fourier Transform function ifft there is a normalization of 1/N. This is the factor that corresponds to the $1/2\pi$ in the real Fourier transform. To make the spectrum look nice in plots we multiply by 1/N. This should of course not be done if the spectrum is used for further calculations since ifft will do this also. Parseval now says that the integral of $|\tilde{A}(\omega)|^2$ should equal the integral of $|A(t)|^2$.

APPENDIX C

Publications

Refereed Articles and Book Chapters

2010 **Multi-channel fiber link for THz imaging systems**, Rasmus Kjelsmark Olsson, Finn Eichhorn, Lasse Høgstedt, Jonas C. D. Buron, Peter Uhd Jepsen, *In preparation.*

2010 **Optical fiber link for transmission of 1-nJ femtosecond laser pulses at 1550 nm**, Finn Eichhorn, Rasmus Kjelsmark Olsson, Jonas C. D. Buron, Lars Grüner-Nielsen, Jens Engholm Pedersen, Peter Uhd Jepsen, *Optics Express*, volume 18, 2010.

2009 **THz Imaging Systems with Aperture Synthesis Techniques**, V. Krozer, T. Löffler, P. U. Jepsen, Finn Eichhorn, Rasmus Kjelsmark Olsson, Jonas C. D. Buron, J. Dall, A. Kusk, V. Zhurbenko, T. Jensen, *submitted to IEEE Trans. Microwave Theory Tech.*, 2009.

2009 **Terahertz technology**, Krzysztof Iwaszczuk, Henrik Porte, Rasmus Kjelsmark Olsson, David Cooke, Dmitry Turchinovich, Peter Uhd Jepsen, *Chapter in Beyond Optical Horizons*, DTU Fotonik, 2009.

Conference Papers

2010 **A multi-element THz imaging system**, F. Eichhorn, L. Høgstedt, J. C. D. Buron, R. K. Olsson, M. Rahbek, A. Kusk, J. Dall, P. U. Jepsen, *Abstract ID 1594374, submitted to 35th International Conference on Infrared, Millimeter, and Terahertz Waves, Rome, Italy*, 2010.

2009 **Low dispersion fiber link for distribution of femtosecond pulses to photonicly driven terahertz emitter and detector units**, Finn Eichhorn, Rasmus K. Olsson, Jonas C. D. Buron, Peter Uhd Jepsen, *1st Nordic Meeting in Physics, Kongens Lyngby, Denmark*, Danish Physical Society (DFS), 2009.

2007 **Femtosecond all-polarization-maintaining fiber laser operating at 1028 nm**, Rasmus K. Olsson, Thomas V. Andersen, Lasse Leick, Vita Levitan, Peter Uhd Jepsen, Dmitry Turchinovich, *Advanced Laser Technologies 2007 (Ivan A. Shcherbakov, Risto Myllyla, Alexander V. Priezzhev, Matti Kinnunen, Vladimir I. Pustovoy, Mikhail Y. Kirillin, Alexey P. Popov, eds.)*, SPIE, volume 7022, 2007.

Refereed Articles not related to the Ph.D. project

2008 **Quantum memory and teleportation using macroscopic gas samples**, J Sherson, H Krauter, R K Olsson, B Julsgaard, E S Polzik, *Journal of Physics B: Atomic, Molecular and Optical Physics*, volume 41, 2008.

2006 **Quantum teleportation between light and matter** Jacob F. Sherson, Hanna Krauter, Rasmus K. Olsson, Brian Julsgaard, Klemens Hammerer, Ignacio Cirac, Eugene S. Polzik, *Nature*, volume 443, 2006.

Bibliography

[1] http://en.wikipedia.org/wiki/Horsepower.

[2] Jonathan C. Knight. Photonic crystal fibres. *Nature*, 424(6950):847–851, 2003.

[3] John M. Dudley and J. Roy Taylor. Ten years of nonlinear optics in photonic crystal fibre. *Nat Photon*, 3(2):85–90, February 2009.

[4] G. P. Agrawal. *Nonlinear Fiber Optics*. Academic Press, 4th edition, 2006.

[5] Amar R. Bhagwat and Alexander L. Gaeta. Nonlinear optics in hollow-core photonic bandgap fibers. *Optics Express*, 16(7):5035–5047, March 2008.

[6] F. Benabid, F. Couny, J. C. Knight, T. A. Birks, and P. St J. Russell. Compact, stable and efficient all-fibre gas cells using hollow-core photonic crystal fibres. *Nature*, 434(7032):488–491, March 2005.

[7] Francois Couny, Olivier Carraz, and Fetah Benabid. Control of transient regime of stimulated raman scattering using hollow-core PCF. *Journal of the Optical Society of America B*, 26(6):1209–1215, June 2009.

[8] Warren R Zipfel, Rebecca M Williams, and Watt W Webb. Nonlinear magic: multiphoton microscopy in the biosciences. *Nat Biotech*, 21(11):1369–1377, November 2003.

[9] Masayoshi Tonouchi. Cutting-edge terahertz technology. *Nat Photon*, 1(2):97–105, February 2007.

[10] Wai Lam Chan, Jason Deibel, and Daniel M Mittleman. Imaging with terahertz radiation. *Reports on Progress in Physics*, 70(8):1325–1379, 2007.

[11] Lars Grüner-Nielsen, Marie Wandel, Poul Kristensen, Carsten Jorgensen, Lene Vilbrad Jorgensen, Bent Edvold, Bera Palsdottir, and Dan Jakobsen. Dispersion-Compensating fibers. *Journal of Lightwave Technology*, 23(11):3566, November 2005.

[12] Chinlon Lin, H. Kogelnik, and L. G. Cohen. Optical-pulse equalization of low-dispersion transmission in single-mode fibers in the 1.3?1.7-μm spectral region. *Optics Letters*, 5(11):476–478, November 1980.

[13] C.-C. Chang, A. M. Weiner, A. M. Vengsarkar, and D. W. Peckham. Broadband fiber dispersion compensation for sub-100-fs pulses with a compression ratio of 300. *Optics Letters*, 21(15):1141–1143, 1996.

[14] D. G. Ouzounov, K. D. Moll, M. A. Foster, W. R. Zipfel, W. W. Webb, and Alexander L. Gaeta. Delivery of nanojoule femtosecond pulses through large-core microstructured fibers. *Optics Letters*, 27(17):1513–1515, 2002.

[15] Julia S. Skibina, Rumen Iliew, Jens Bethge, Martin Bock, Dorit Fischer, Valentin I. Beloglasov, Reiner Wedell, and Gunter Steinmeyer. A chirped photonic-crystal fibre. *Nat Photon*, 2(11):679–683, November 2008.

[16] Georges Humbert, J. Knight, G. Bouwmans, P. Russell, D. Williams, P. Roberts, and B. Mangan. Hollow core photonic crystal fibers for beam delivery. *Optics Express*, 12(8):1477–1484, April 2004.

[17] Matthew G. Welch, Charles E. de Nobriga, Rodrigo Amezcua Correa, William J. Wadsworth, and Jonathan C. Knight. Accurate measurement of the dispersion of hollow-core fibers using a scalable technique. *Optics Express*, 17(11):9006–9012, May 2009.

[18] Matthew G. Welch, Kevin Cook, Rodrigo Amezcua Correa, Frederic Gerome, WilliamJ. Wadsworth, AndreyV. Gorbach, DmitryV. Skryabin, and JonathanC. Knight. Solitons in hollow core photonic crystal fiber: Engineering nonlinearity and compressing pulses. *Journal of Lightwave Technology*, 27(11):1644–1652, June 2009.

[19] J. K. Lyngsoe, B. J. Mangan, C. Jakobsen, and P. J. Roberts. 7-cell core hollow-core photonic crystal fibers with low loss in the spectral region around 2 um. *Optics Express*, 17(26):23468–23473, December 2009.

[20] B. Mangan, J. K. Lyngsoe, and P. J. Roberts. Realization of low loss and polarization maintaining hollow core photonic crystal fibers. In *Conference on Lasers and Electro-Optics (CLEO)*, page JFG4, 2008.

[21] J. K. Lyngsoe, B. J. Mangan, and P. J. Roberts. Polarization maintaining hybrid TIR/Bandgap All-Solid photonic crystal fiber. In *Conference on Lasers and Electro-Optics (CLEO)*, page CThV1, 2008.

[22] Dimitre G. Ouzounov, Faisal R. Ahmad, Dirk Muller, Natesan Venkataraman, Michael T. Gallagher, Malcolm G. Thomas, John Silcox, Karl W. Koch, and Alexander L. Gaeta. Generation of megawatt optical solitons in Hollow-Core photonic Band-Gap fibers. *Science*, 301(5640):1702–1704, September 2003.

[23] F. Luan, J. Knight, P. Russell, S. Campbell, D. Xiao, D. Reid, B. Mangan, D. Williams, and P. Roberts. Femtosecond soliton pulse delivery at 800nm wavelength in hollow-core photonic bandgap fibers. *Optics Express*, 12(5):835–840, March 2004.

[24] F. Gerome, P. Dupriez, J. Clowes, J. C. Knight, and W. J. Wadsworth. High power tunable femtosecond soliton sourceusing hollow-core photonic bandgap fiber, andits use for frequency doubling. *Optics Express*, 16(4):2381–2386, February 2008.

[25] F. Gerome, K. Cook, A. K. George, W. J. Wadsworth, and J. C. Knight. Delivery of sub-100fs pulses through 8m of hollow-core fiber using soliton compression. *Optics Express*, 15(12):7126–7131, June 2007.

[26] Jesper T. Kristensen, Andreas Houmann, Xiaomin Liu, and Dmitry Turchinovich. Low-loss polarization-maintaining fusion splicing of single-mode fibers and hollow-core photonic crystal fibers, relevant for monolithic fiber laser pulse compression. *Optics Express*, 16(13):9986–9995, June 2008.

[27] Dmitry Turchinovich, Xiaomin Liu, and Jesper Laegsgaard. Monolithic all-PM femtosecond yb-fiber laser stabilized with a narrow-band fiber bragg grating and pulse-compressed in a hollow-core photonic crystal fiber. *Optics Express*, 16(18):14004–14014, 2008.

[28] J. Laegsgaard and P. J. Roberts. Dispersive pulse compression in hollow-core photonic bandgap fibers. *Optics Express*, 16(13):9628–9644, June 2008.

[29] Jesper Laegsgaard and Peter John Roberts. Compression of realistic laser pulses in hollow-core photonic bandgap fibers. *Journal of the Optical Society of America B*, 26(4):783–791, April 2009.

[30] Jesper Laegsgaard and Peter John Roberts. Influence of air pressure on soliton formation in hollow-core photonic bandgap fibers. *Journal of the Optical Society of America B*, 26(9):1795–1800, 2009.

[31] Jesper Laegsgaard and Peter John Roberts. Theory of adiabatic pressure-gradient soliton compression in hollow-core photonic bandgap fibers. *Optics Letters*, 34(23):3710–3712, December 2009.

[32] Andrey V. Gorbach and Dmitry V. Skryabin. Soliton self-frequency shift, non-solitonicradiation and self-induced transparencyin air-core fibers. *Optics Express*, 16(7):4858–4865, March 2008.

[33] http://www.photonics.umd.edu/software/ssprop/.

[34] W. J. Tomlinson, R. H. Stolen, and A. M. Johnson. Optical wave breaking of pulses in nonlinear optical fibers. *Optics Letters*, 10(9):457–459, 1985.

[35] Rick Trebino, Kenneth W. DeLong, David N. Fittinghoff, John N. Sweetser, Marco A. Krumbugel, Bruce A. Richman, and Daniel J. Kane. Measuring ultrashort laser pulses in the time-frequency domain using frequency-resolved optical gating. *Review of Scientific Instruments*, 68(9):3277, 1997.

[36] K. W. DeLong, Rick Trebino, and Daniel J. Kane. Comparison of ultrashort-pulse frequency-resolved-optical-gating traces for three common beam geometries. *Journal of the Optical Society of America B*, 11(9):1595–1608, 1994.

[37] Rick Trebino. *Frequency-Resolved Optical Gating: The Measurement of Ultrafast Laser Pulses*. Kluwer Academic Publishers, 2000.

[38] K. W. DeLong, Rick Trebino, J. Hunter, and W. E. White. Frequency-resolved optical gating with the use of second-harmonic generation. *Journal of the Optical Society of America B*, 11(11):2206–2215, November 1994.

[39] Daniel J. Kane and Rick Trebino. Single-shot measurement of the intensity and phase of an arbitrary ultrashort pulse by using frequency-resolved optical gating. *Optics Letters*, 18(10):823–825, May 1993.

[40] John M. Dudley, Ian A. Walmsley, and Rick Trebino. Measurement of ultrashort electromagnetic pulses. *Journal of the Optical Society of America B*, 25(6):MU1–MU2, June 2008.

[41] Xun Gu, Lin Xu, Mark Kimmel, Erik Zeek, Patrick O?Shea, Aparna P. Shreenath, Rick Trebino, and Robert S. Windeler. Frequency-resolved optical gating and single-shot spectral measurements reveal fine structure in microstructure-fiber continuum. *Optics Letters*, 27(13):1174–1176, July 2002.

[42] John Dudley, Xun Gu, Lin Xu, Mark Kimmel, Erik Zeek, Patrick O'Shea, Rick Trebino, Stephane Coen, and Robert Windeler. Cross-correlation frequency resolved optical gating analysis of broadband continuum generation in photonic crystal fiber: simulations and experiments. *Optics Express*, 10(21):1215–1221, October 2002.

[43] Anatoly Efimov and Antoinette J. Taylor. Cross-correlation frequency-resolved optical gating for studying ultrashort-pulse nonlinear dynamics in arbitrary fibers. *Applied Optics*, 44(20):4408–4411, July 2005.

[44] J. M. Dudley, L. P. Barry, P. G. Bollond, J. D. Harvey, and R. Leonhardt. Characterizing pulse propagation in optical fibers around 1550 nm using Frequency-Resolved optical gating. *Optical Fiber Technology*, 4(3):237–265, July 1998.

[45] J. M. Dudley, L. P. Barry, J. D. Harvey, M.D. Thomson, B.C. Thomsen, P. G. Bollond, and R. Leonhardt. Complete characterization of ultrashort pulse sources at 1550 nm. *IEEE Journal of Quantum Electronics*, 35(4):441–450, 1999.

[46] Balakishore Yellampalle, KiYong Kim, and Antoniette J. Taylor. Amplitude ambiguities in second-harmonic generation frequency-resolved optical gating. *Optics Letters*, 32(24):3558–3560, December 2007.

[47] Balakishore Yellampalle, KiYong Kim, and Antoniette J. Taylor. Amplitude ambiguities in second-harmonic generation frequency-resolved optical gating: erratum. *Optics Letters*, 33(23):2854, December 2008.

[48] Lina Xu, Daniel J. Kane, and Rick Trebino. Amplitude ambiguities in second-harmonic-generation frequency-resolved optical gating: comment. *Optics Letters*, 34(17):2602, 2009.

[49] Balakishore Yellampalle, KiYong Kim, and Antoinette J. Taylor. Amplitude ambiguities in second-harmonic-generation frequency-resolved optical gating: reply to comment. *Optics Letters*, 34(17):2603, 2009.

[50] K.W. DeLong, D.N. Fittinghoff, and R. Trebino. Practical issues in ultrashort-laser-pulse measurement using frequency-resolved optical gating. *IEEE Journal of Quantum Electronics*, 32(7):1253–1264, 1996.

[51] http://www.femtosoft.biz/frog.shtml.

[52] http://www.mathworks.com/matlabcentral/fileexchange/16235-frequency-resolved-optical-gating-frog.

[53] Daniel J. Kane. Real-time measurement of ultrashort laser pulses using principal component generalized projections. *Selected Topics in Quantum Electronics, IEEE Journal of*, 4(2):278–284, 1998.

[54] Daniel J. Kane. Principal components generalized projections: a review [Invited]. *Journal of the Optical Society of America B*, 25(6):A120–A132, June 2008.

[55] Rasmus K. Olsson, Thomas V. Andersen, Lasse Leick, Vita Levitan, Peter Uhd Jepsen, and Dmitry Turchinovich. Femtosecond all-polarization-maintaining fiber laser operating at 1028 nm. In Ivan A. Shcherbakov, Risto Myllyla, Alexander V. Priezzhev, Matti Kinnunen, Vladimir I. Pustovoy, Mikhail Y. Kirillin, and Alexey P. Popov, editors, *Advanced Laser Technologies 2007*, volume 7022, pages 70221E–5, Levi, Finland, 2007. SPIE.

[56] H. Lim, F. Ö. Ilday, and F. W. Wise. Generation of 2-nJ pulses from a femtosecond ytterbium fiber laser. *Optics Letters*, 28(8):660–662, April 2003.

[57] C. Nielsen, B. Ortac, T. Schreiber, J. Limpert, R. Hohmuth, W. Richter, and A. Tunnermann. Self-starting self-similar all-polarization maintaining yb-doped fiber laser. *Optics Express*, 13(23):9346–9351, November 2005.

[58] F. Ilday, J. Buckley, L. Kuznetsova, and F. Wise. Generation of 36-femtosecond pulses from a ytterbium fiber laser. *Optics Express*, 11(26):3550–3554, December 2003.

[59] K. Sala, G. Kenney-Wallace, and G. Hall. CW autocorrelation measurements of picosecond laser pulses. *IEEE Journal of Quantum Electronics*, 16(9):990–996, 2003.

[60] Finn Eichhorn, Rasmus Kjelsmark Olsson, Jonas C. D. Buron, Lars Grüner-Nielsen, Jens Engholm Pedersen, and Peter Uhd Jepsen. Optical fiber link for transmission of 1-nJ femtosecond laser pulses at 1550 nm. *Optics Express*, 18(7):6978–6987, March 2010.

[61] J. V. Rudd, D. A. Zimdards, and M. W. Warmuth. Compact fiber-pigtailed terahertz imaging system. *Proc. SPIE*, 3934:27–35, 2000.

[62] I. Duling and D. Zimdars. Compact TD-THz systems offer flexible, turnkey imaging solutions. *Laser Focus World*, 43(63), 2007.

[63] B. Sartorius, H. Roehle, H. Künzel, J. Böttcher, M. Schlak, D. Stanze, H. Venghaus, and M. Schell. All-fiber terahertz time-domain spectrometer operating at 1.5 μm telecom wavelengths. *Optics Express*, 16(13):9565–9570, June 2008.

[64] V. Krozer, T. Löffler, P. U. Jepsen, Finn Eichhorn, Rasmus Kjelsmark Olsson, Jonas C. D. Buron, J. Dall, A. Kusk, V. Zhurbenko, and T. Jensen. THz imaging systems with aperture synthesis techniques. *submitted to IEEE Trans. Microwave Theory Tech.*, 2009.

[65] S. Dexheimer. *Terahertz Spectroscopy: Principles and applications.* CRC Press, 2008.

[66] John M. Dudley, Goery Genty, and Stephane Coen. Supercontinuum generation in photonic crystal fiber. *Reviews of Modern Physics*, 78(4):1135, October 2006.